Title

Advances in Thermoelastic Dissipation and Anchor Loss in MEMS Resonators

Permalink

https://escholarship.org/uc/item/7vs9t69j

Author

Lake, Jonathan James

Publication Date

2015

Peer reviewed|Thesis/dissertation

UNIVERSITY OF CALIFORNIA

Los Angeles

Advances in Thermoelastic Dissipation and
Anchor Loss in Micromechanical Resonators

A dissertation submitted in partial satisfaction of the requirements for the degree
Doctor of Philosophy in Electrical Engineering

by

JONATHAN JAMES LAKE

2015

Abstract

Silicon Microelectromechanical (MEMS) resonators are being developed for a wide variety of applications including frequency reference applications, positioning systems (gyroscopes) force sensors (AFM) and energy harvesters. In these applications, energy dissipation greatly influences device performance. For example, in a frequency filter the dissipation will determine the bandwidth of the filter. Many applications require dissipation to be minimized and all applications require accurate characterization of dissipation. In recent years, advanced modeling techniques for some energy loss mechanisms (e.g., thermoelastic dissipation) have been introduced to predict resonator performance based on fundamental physics. The resonator can lose energy through a variety of energy pathways including air damping, losses through the anchor, surface dissipation, resistive damping and thermoelastic dissipation (TED). As modeling techniques improve more and more, dissipation mechanisms can be predicted a proiri, saving significant cost in fabrication trial and error. TED, air damping and resistive damping have accurate models, however, significant work remains to develop accurate general models for anchor loss and surface dissipation.

This work provides a dual approach to MEMS resonator design. For resonators limited by TED, or any loss mechanism that can currently be modeled, this work leverages a new bio-inspired design optimization approach called binary particle swarm optimization (BPSO) used to optimize energy dissipation in MEMS resonators. BPSO produces mask ready designs that minimize damping. This approach was used to optimize low TED resonators and resulted in a measured 33% improvement over the previous intuitive design approach. Secondly, in order to address the lack of an accurate general model for anchor loss, this work introduces a novel anchor loss modeling approach independent of resonator frequency and shown to be accurate across 2 orders of magnitude in frequency. The main goal of this work is to encourage the MEMS community to move away from a trial and error fabrication approach and leverage modern modeling and optimization techniques to design high performance resonators.

The dissertation of Jonathan James Lake is approved

Oscar M. Stafsudd

Nasr M. Ghoniem

Robert N. Candler, Committee Chair

University of California, Los Angeles

2015

Dedication

I dedicate this work to my late father Ralph Lake

Table of Contents

Table of Figures

Acknowledgements

Biography

Jonathan Lake received the B.S. degree with distinction in general engineering from Harvey Mudd College, Claremont, CA, USA in 2009, and the M.S. degree in electrical engineering from University of California, Los Angeles (UCLA), CA, USA in 2012. His Masters was completed working under Professor Robert Candler in the Sensors and Technology Laboratory. His research involved the study of fundamental dissipation mechanisms in resonant sensors. His current research interests include microelectromechanical systems modeling and simulation, swarm intelligence and optimization theory. He has also spent over two summers working at HRL Laboratories, Malibu, CA where he was with the Sensors and Materials Laboratory

Chapter 1 Introduction

Energy Dissipation in Resonators

Nano- and micro-electromechanical Systems (N/MEMS) resonators have a broad set of commercial and

scientific uses. For commercial applications, these miniaturized resonators are used as gyroscopes in

automotive safety systems [1, 2] and as timing references and frequency filters in cell phones, computers,

and video games [3-11]. In research, resonators have been used as highly sensitive chemical and

biological sensors [12-17] and have been investigated as future low-power replacements of CMOS

switches [18, 19]. As measurement tools, resonators can detect mass with zeptogram resolution [12, 20,

and 21], a single electron spin [22], and quantum ground state [23, 24]. Despite their wide range of uses,

these resonator-based systems all share a common limitation in that their performance is inherently

limited by the amount of energy lost in the resonator. To gain an understanding of energy dissipation on

the dynamics of a resonator, one can imagine a resonator that is driven into steady-state resonance by a

sinusoidal driving force. If the force driving the resonator is removed, the amplitude will decay (*i.e.*,

energy will be dissipated) as shown in Figure 1.
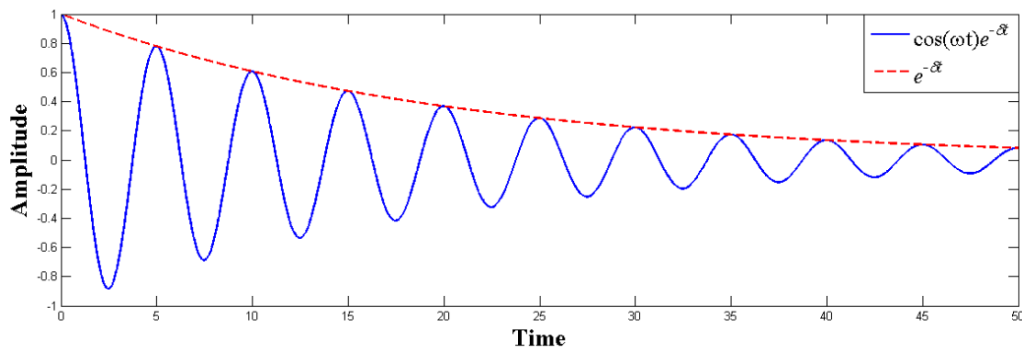
Figure 1: Damped oscillation, described by $x(t) = \cos(\omega t)e^{-\delta t}$, where x(t) is the displacement, ω is the angular frequency of oscillation, and δ is the damping factor.

For systems with minimal damping ($\delta \ll \omega$), it can be assumed that ω is very close to the undamped resonant frequency, ω_o. The quality factor, Q, is frequently used to describe the energy loss in the system and is defined as

$$Q = 2\pi \frac{W_{Stored}}{W_{Lost}} = \frac{\omega_o}{2\delta} \qquad (1)$$

Where W_{Stored} is the total energy stored in the resonator, and W_{Lost} is the energy lost in one cycle of vibration. The vibration amplitude peaks at resonance, and a measure of the width of the peak at half maximum amplitude (see Figure 2) is related to the quality factor as follow

$$Q = 2\pi \frac{W_{Stored}}{W_{Lost}} = \frac{\omega_o}{\Delta \omega} \qquad (2)$$
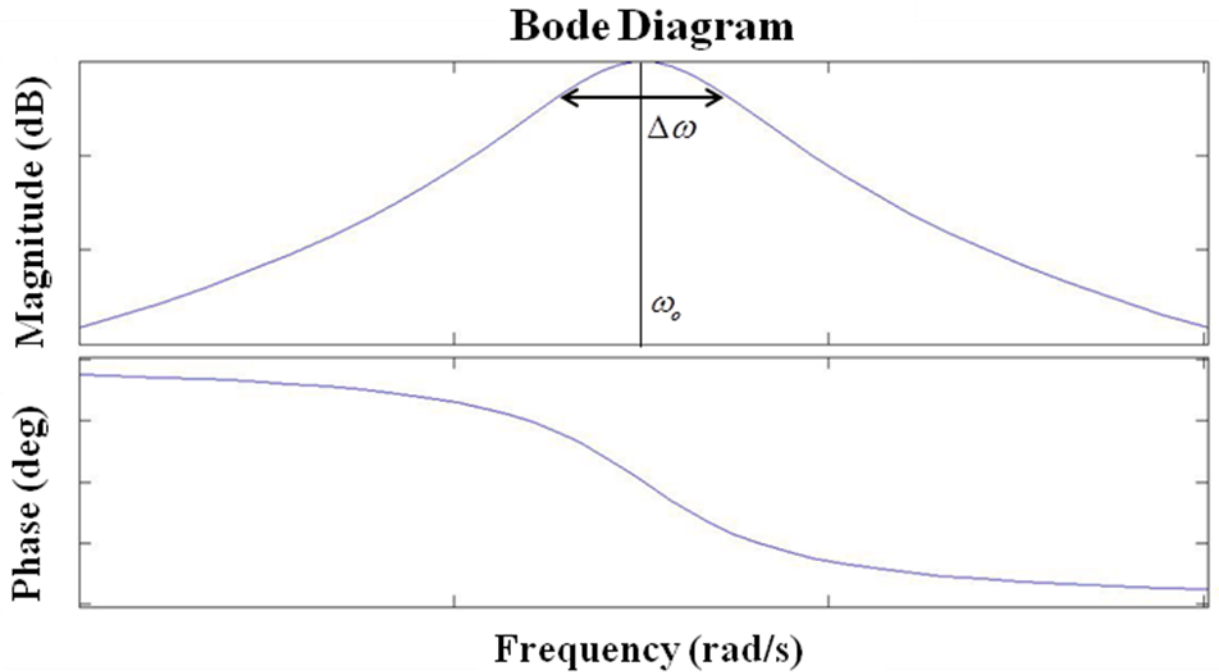
Bode Diagram

Figure 2: Bode diagram of a damped resonator. Bandwidth ($\Delta\omega$) is the full width at half maximum due to damping.

There are many mechanisms by which a resonator can dissipate energy during vibration. The most common are summarized in table 1. The Q can also be determined by measuring the bandwidth ($\Delta\omega$) from the phase (defined as the frequency range between -45 and -135 degrees.

2

Table 1: Energy dissipation mechanisms in N/MEMS resonators**.**

Energy Loss	Description
Thermoelastic	Coupled thermomechanics in a resonator causes energy dissipation. Dynamic strain gradient generates a temperature gradient. Energy is dissipated when heat flows to equilibrate temperature.
Surface	General term describing surface-dependent energy loss. More prevalent in nanoscale structures, where surface area to volume ratio is large.
Landau-Rumer	Phonon-phonon coupling that occurs when phonon populations are disturbed from equilibrium. Valid when acoustic wavelength is less than phonon mean free path.
Akhieser	Phonon-phonon coupling that occurs when phonon populations are disturbed from equilibrium. Valid when acoustic wavelength is greater than phonon mean free path.
Clamping	Acoustic waves travel through the resonator anchor and do not return.
Fluid	Vibrating resonator transfers mechanical energy to surrounding air or liquid molecules.
Resistive	Energy lost when resonator is used to drive signal across resistive load.

Assuming these energy losses add linearly, which is true for small losses, an equation can be derived

relating the loss from a single mechanism, described by Q_i, to the overall system loss

$$\frac{1}{Q_{System}} = \sum_i \frac{1}{Q_i} = \frac{1}{Q_{fluid}} + \frac{1}{Q_{thermoelastic}} + \frac{1}{Q_{clamping}} + \frac{1}{Q_{surface}} \dots \tag{3}$$

At atmospheric pressures, fluidic damping is generally the dominant dissipation mechanism. However,

other dissipation mechanisms will dominate when the resonator is operated in a vacuum or at high

frequencies. The focus of this thesis is the theory and current advances in the application of thermoelastic

dissipation (TED) and anchor loss.

Current Knowledge

Currently, many dissipation mechanisms are well understood and accurate predictive models have been developed. These include thermoelastic, Akhieser, Landau Rumer, fluid and resistive dissipation. However a fully general 3D model for clamping and surface dissipation remains an area of significant study (Figure 3). Currently device Q performance is typically analyzed with a trial and error approach.
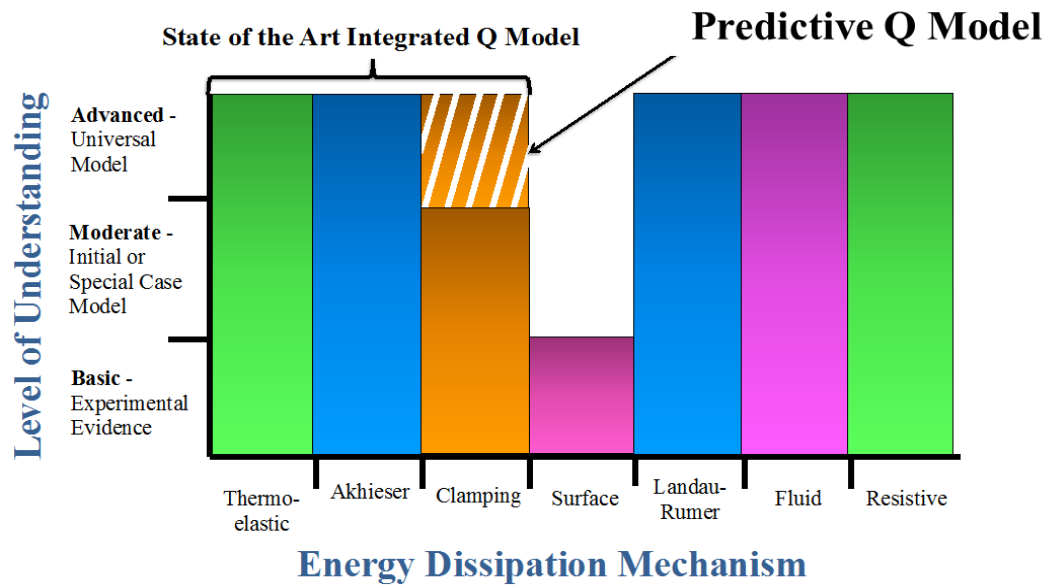
Figure 3: Current knowledge of common dissipation mechanisms. A goal in the MEMS community is to move away from the expensive trial and error approach by creating a predictive Q model to model design performance.

This approach is very costly due to steep fabrication costs. This thesis presents a modern bio-inspired design method to minimize TED and presents a novel fully general 3D model for anchor loss. The aim of this work is to move beyond trial and error and use advanced design techniques in an effort to alleviate pressures on fabrication technologies.

Chapter 2 discusses theory of thermoelastic dissipation from a fully coupled and weakly coupled perspective. Chapter 3 provides background on anchor losses. Chapter 4 focuses on the Particle swarm optimization algorithm. Chapter 5 provides an overview of the epi-seal fabrication process. Chapter 6 outlines the experimental study approach. Chapter 7 discusses experimental results from resonators

designed to specifically study anchor damping and thermoelastic dissipation. Chapter 8 includes additional studies on both TED and anchor loss and Chapter 9 finishes with conclusions of this work.

Chapter 2 Thermoelastic Dissipation Theory

Introduction

Thermoelastic dissipation (TED) describes the process where the mechanical energy of a vibrating resonator is irreversibly converted to thermal energy. A derivation is presented that describes the fully-coupled thermal-mechanical physics that lead to TED. An alternative approach, the weakly-coupled approach, is also presented in order to illustrate the coupling of a mechanical eigenmode with multiple thermal eigenmodes. In the last section, both the fully-coupled and weakly-coupled modeling approaches are utilized to design resonators with low TED.

Theory

Clarence Zener contributed much of the early, defining work on thermoelastic dissipation (TED) [25, 26], which arises from the coupling between mechanical and thermal domains. The following sentences describe the thermal-mechanical coupling process that causes TED. Thermal expansion, a well-known phenomenon, occurs when a change in temperature produces a change in the dimensions of a solid. This interaction between mechanical and thermal domains also works in the other direction. That is, a solid that is strained will experience a change in temperature. For most materials, including silicon, compressive strain will cause the material temperature to increase, while tensile strain will cause temperature to decrease. The strain gradient that occurs across a flexing beam gives rise to a temperature gradient across the beam. If heat flows to relax the temperature gradient as shown in Figure 4, thermoelastic dissipation occurs as the vibration energy is irreversibly converted to heat. Another way to state this is that mechanical energy is used to create a temperature gradient, causing an exchange between system energy and entropy. Heat flows to equilibrate the temperature gradient, and the energy stored in entropy is irrecoverably lost.
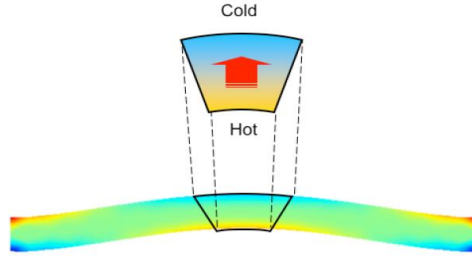
Figure 4: Thermal gradients within a flexing beam produce irreversible heat transfer leading to thermoelastic dissipation.

Numerical Solutions to the Fully-Coupled TED equations

The full derivations of the coupled equations that govern thermoelastic vibrations in a solid are available in other literature [27]. Here, the fundamental principles of this derivation are presented for 3-D resonators. These equations can be numerically solved in 2-D and 3-D by finite-element solvers that are capable of solving partial differential equations. The finite element method is especially useful for complex geometries, which are very difficult to model analytically.

Governing Equations in 3-D

Mechanics Equation

To obtain the coupled thermal-mechanical dynamics, the constitutive relation (eq. 7) will be applied to the force balance constraints and Fourier's law of heat transfer, as described in the following section. The force (F) on a unit cube of length dx, dy, dz can be related to stress (σ) by

$$F_i = \left(\frac{\partial \sigma_{i1}}{\partial x} + \frac{\partial \sigma_{i2}}{\partial y} + \frac{\partial \sigma_{i3}}{\partial z} \right) dxdydz \tag{4}$$

Here, σ_{ij} is the stress in the i direction acting on a plane perpendicular to the j axis (where $\sigma_{11}=\sigma_{xx}$ etc.). Thus, cases where $i \neq j$ represent shear stress. Eq. 4 can be related to the equation of motion (eq. 5), where ρ is the density of the resonator material and u_i is the displacement in the i direction.

$$\rho \frac{\partial^2 u_i}{\partial t^2} dxdydz = \left(\frac{\partial \sigma_{i1}}{\partial x} + \frac{\partial \sigma_{i2}}{\partial y} + \frac{\partial \sigma_{i3}}{\partial z} \right) dxdydz \tag{5}$$

The stiffness matrices are symmetric assuming there is no rotational acceleration, and a reduced tensor notation can be used (sometimes referred to as Voight notation).

$$\sigma_1 = \sigma_{11} = \sigma_{xx}; \quad \sigma_2 = \sigma_{22} = \sigma_{yy}; \quad \sigma_3 = \sigma_{33} = \sigma_{zz}; \quad \sigma_4 = \sigma_{23} = \sigma_{32} = \sigma_{yz} = \sigma_{zy};$$
$$\sigma_5 = \sigma_{13} = \sigma_{31} = \sigma_{xz} = \sigma_{zx}; \quad \sigma_6 = \sigma_{12} = \sigma_{21} = \sigma_{xy} = \sigma_{yx} \tag{6}$$

The constitutive equation describes the impact of temperature on stress in the material and is given by

$$\sigma_i = c_{ij}\varepsilon_j - \alpha(3\lambda + 2\mu)T\delta_{ij} \tag{7}$$

Where c is the stiffness matrix, ε is strain, μ and λ are lamè parameters, α is the coefficient of thermal expansion, T is temperature, and δ_{ij} is the Kronecker delta function, which is equal to one when $i = j$ and is zero otherwise. In matrix form, equation 7 becomes

$$\begin{bmatrix} \sigma_1 \\ \sigma_2 \\ \sigma_3 \\ \sigma_4 \\ \sigma_5 \\ \sigma_6 \end{bmatrix} = \begin{bmatrix} \lambda + 2\mu & \lambda & \lambda & 0 & 0 & 0 \\ \lambda & \lambda + 2\mu & \lambda & 0 & 0 & 0 \\ \lambda & \lambda & \lambda + 2\mu & 0 & 0 & 0 \\ 0 & 0 & 0 & \mu & 0 & 0 \\ 0 & 0 & 0 & 0 & \mu & 0 \\ 0 & 0 & 0 & 0 & 0 & \mu \end{bmatrix} \begin{bmatrix} \varepsilon_1 \\ \varepsilon_2 \\ \varepsilon_3 \\ \varepsilon_4 \\ \varepsilon_5 \\ \varepsilon_6 \end{bmatrix} - (3\lambda + 2\mu)T \begin{bmatrix} \alpha \\ \alpha \\ \alpha \\ 0 \\ 0 \\ 0 \end{bmatrix} \tag{8}$$

The force balance equation in the x-direction is

$$\rho \frac{\partial^2 u}{\partial t^2} = \left(\frac{\partial \sigma_{11}}{\partial x} + \frac{\partial \sigma_{12}}{\partial y} + \frac{\partial \sigma_{13}}{\partial z} \right) \tag{9}$$

The equations for stress (eq. 8) are substituted into the force balance equation (eq. 9) to give

$$\rho \frac{\partial^2 u}{\partial t^2} = \lambda \frac{\partial}{\partial x}\left(\varepsilon_1 + \varepsilon_2 + \varepsilon_3 \right) + 2\mu \frac{\partial}{\partial x} \varepsilon_1 + \mu \frac{\partial}{\partial y} \varepsilon_6 + \mu \frac{\partial}{\partial z} \varepsilon_5 - \alpha(3\lambda + 2\mu)\frac{\partial T}{\partial x} \tag{10}$$

The strain displacement relationships are represented using reduced tensor notation

$$\varepsilon_1 = \frac{\partial u}{\partial x}; \quad \varepsilon_2 = \frac{\partial v}{\partial y}; \quad \varepsilon_3 = \frac{\partial w}{\partial z}; \quad \varepsilon_4 = \frac{\partial v}{\partial z} + \frac{\partial w}{\partial y}; \quad \varepsilon_5 = \frac{\partial u}{\partial z} + \frac{\partial w}{\partial x}; \quad \varepsilon_6 = \frac{\partial u}{\partial y} + \frac{\partial v}{\partial x} \tag{11}$$

Substituting displacement for strain and simplifying, the equation of motion in the x-direction (eq. 10) becomes

$$\rho \frac{\partial^2 u}{\partial t^2} = \mu \left(\frac{\partial^2 u}{\partial x^2} + \frac{\partial^2 u}{\partial y^2} + \frac{\partial^2 u}{\partial z^2} \right) + (\lambda + \mu)\left(\frac{\partial^2 u}{\partial x^2} + \frac{\partial^2 v}{\partial x \partial y} + \frac{\partial^2 w}{\partial x \partial z} \right) - \alpha(3\lambda + 2\mu)\frac{\partial T}{\partial x} \tag{12}$$

The expressions for the y and z directions are similar and can be found in Table 2.

Heat Equation

The last equation to derive is the coupled heat equation. Fourier's law in terms of entropy is used to derive the heat equation.

$$T\dot{S} = \kappa \nabla^2 T \tag{13}$$

T is again temperature, S is entropy and κ is thermal conductivity (isotropic).

The constitutive relation for entropy is

$$S = \alpha c \varepsilon + \frac{C_v}{T_{init}} T \qquad (14)$$

T_{init} is the ambient temperature, and C_v is the heat capacity per unit volume.

The constitutive relation for entropy in matrix form is

$$S = \begin{bmatrix} \alpha & \alpha & \alpha & 0 & 0 & 0 \end{bmatrix} \begin{bmatrix} \lambda + 2\mu & \lambda & \lambda & 0 & 0 & 0 \\ \lambda & \lambda + 2\mu & \lambda & 0 & 0 & 0 \\ \lambda & \lambda & \lambda + 2\mu & 0 & 0 & 0 \\ 0 & 0 & 0 & \mu & 0 & 0 \\ 0 & 0 & 0 & 0 & \mu & 0 \\ 0 & 0 & 0 & 0 & 0 & \mu \end{bmatrix} \begin{bmatrix} \varepsilon_1 \\ \varepsilon_2 \\ \varepsilon_3 \\ \varepsilon_4 \\ \varepsilon_5 \\ \varepsilon_6 \end{bmatrix} + \frac{C_v}{T_{init}} T \qquad (15)$$

The matrix of equation 15 is reduced to

$$S = \alpha(3\lambda + 2\mu)(\varepsilon_1 + \varepsilon_2 + \varepsilon_3) + \frac{C_v}{T_{init}} T \qquad (16)$$

Substituting this constitutive relation into Fourier's Law (eq. 13) gives

$$T\left[\alpha(3\lambda + 2\mu)(\dot{\varepsilon}_1 + \dot{\varepsilon}_2 + \dot{\varepsilon}_3) + \frac{C_v}{T_{init}} \dot{T} \right] = \kappa \nabla^2 T \qquad (17)$$

Linearizing at the equilibrium temperature T_{init} yields

$$\kappa \nabla^2 T - C_v \dot{T} - \underbrace{\alpha(3\lambda + 2\mu) T_{init}(\dot{\varepsilon}_1 + \dot{\varepsilon}_2 + \dot{\varepsilon}_3)}_{Source\ term} = 0 \qquad (18)$$

This equation is combined with the three mechanics equations and completes the set of coupled equations.

These equations are shown in Table 2.

Table 2: Coupled equations for calculating thermoelastic dissipation.

Heat equation	$\kappa\nabla^2 T - C_v\dot{T} - \alpha(3\lambda + 2\mu)T_{init}(\dot{\varepsilon}_1 + \dot{\varepsilon}_2 + \dot{\varepsilon}_3) = 0$
Mechanics (x direction)	$\rho\dfrac{\partial^2 u}{\partial t^2} = \mu\left(\dfrac{\partial^2 u}{\partial x^2} + \dfrac{\partial^2 u}{\partial y^2} + \dfrac{\partial^2 u}{\partial z^2}\right) + (\lambda + \mu)\left(\dfrac{\partial^2 u}{\partial x^2} + \dfrac{\partial^2 v}{\partial x\partial y} + \dfrac{\partial^2 w}{\partial x\partial z}\right) - \alpha(3\lambda + 2\mu)\dfrac{\partial T}{\partial x}$
Mechanics (y direction)	$\rho\dfrac{\partial^2 v}{\partial t^2} = \mu\left(\dfrac{\partial^2 v}{\partial x^2} + \dfrac{\partial^2 v}{\partial y^2} + \dfrac{\partial^2 v}{\partial z^2}\right) + (\lambda + \mu)\left(\dfrac{\partial^2 u}{\partial y\partial x} + \dfrac{\partial^2 v}{\partial y^2} + \dfrac{\partial^2 w}{\partial y\partial z}\right) - \alpha(3\lambda + 2\mu)\dfrac{\partial T}{\partial y}$
Mechanics (z direction)	$\rho\dfrac{\partial^2 w}{\partial t^2} = \mu\left(\dfrac{\partial^2 w}{\partial x^2} + \dfrac{\partial^2 w}{\partial y^2} + \dfrac{\partial^2 w}{\partial z^2}\right) + (\lambda + \mu)\left(\dfrac{\partial^2 u}{\partial z\partial x} + \dfrac{\partial^2 v}{\partial z\partial y} + \dfrac{\partial^2 w}{\partial z^2}\right) - \alpha(3\lambda + 2\mu)\dfrac{\partial T}{\partial z}$

These four, coupled equations can be solved as an eigenvalue problem to determine the resonant frequency and damping of a structure. Finite element software can be used to solve these equations for a complex geometry. The generalized eigenvalues, ω_i, of these equations are complex. The imaginary components represent the mechanical vibration frequency while the real part provides the rate of decay, δ, for an unforced vibration due to thermal coupling. The quality factor of the resonator is given by dividing the real and imaginary components of the eigenvalues as follows:

$$Q_i = \frac{\mathbf{Im}\{\omega_i\}}{2\,\mathbf{Re}\{\omega_i\}} \tag{19}$$

Plane Stress Approximation

It can be beneficial to use a plane stress approximation, which allows the coupled equations to be solved in two dimensions instead of three. A summary of the plane stress approximation may be found in

10

supporting literature [28]. The plane stress approximation can be used when the geometry of the device is very thin in one dimension relative to the others.

$$L_z << L_x, L_y \qquad (20)$$

For thin plates, $\sigma_3, \sigma_4, \sigma_5$ can be approximated as zero, and the remaining stress terms, $\sigma_1, \sigma_2, \sigma_6,$ may be assumed to have no **z** dependence.

$$\sigma_3 = \sigma_4 = \sigma_5 = 0$$
$$\frac{\partial \sigma_1}{\partial z} = \frac{\partial \sigma_2}{\partial z} = \frac{\partial \sigma_6}{\partial z} = 0 \qquad (21)$$

With these assumptions, similar to the derivation shown above for the 3D case, the coupled equations in 2 dimensions can be derived. These equations can be found in supporting literature [29].

Weakly Coupled Approach

An alternative to solving the fully coupled equations simultaneously is to solve the mechanical and thermal equations separately and use the spatial overlap of the solutions in order to approximate thermoelastic coupling. This alternative method utilizes a weakly-coupled approach developed by Zener [25,26]. This approach is generalized to apply to an arbitrary geometry. While Zener's weakly-coupled approach is not as accurate as solving the fully-coupled equations, it offers further insight into thermoelastic dynamics, specifically how mechanical modes couple with thermal modes to produce damping. The insight gained in the weakly-coupled approach can be used to guide the design of a resonator to minimize energy lost from TED.

Thermal Eigenmodes

In order to present the weakly-coupled approach to solving thermoelastic dissipation, the concept of *thermal eigenmodes* must be introduced. Thermal eigenmodes are analogous to *mechanical eigenmodes*,

which are familiar and are commonly studied. Mechanical eigenmodes are derived from the homogeneous mechanical equation, which is a form of Newton's first law. The homogenous mechanical equation is given below in equation 22. The 1-D equation is used here for simplicity.

$$\rho \frac{\partial^2 \boldsymbol{u}}{\partial \boldsymbol{t}^2} = \nabla \cdot \sigma \tag{22}$$

The eigenmodes (solutions) of this equation are the familiar mode shapes represented on the left in Figure 5. These deformations vary as a sinusoid with time. An analogous approach can be used to solve for thermal eigenmodes. Thermal eigenmodes are solved using the homogenous heat equation for conduction.

$$k\nabla^2 \boldsymbol{T} = C_v \frac{\partial \boldsymbol{T}}{\partial \boldsymbol{t}} \tag{23}$$

Using separation of variables, this can be written as the Helmholtz equation.

$$k\nabla^2 v_i(x, y, z) + \lambda_i C_v v_i(x, y, z) = 0 \tag{24}$$

Where v_i is the eigensolution (or eigenmode) and λ_i is the eigenvalue (also referred to as thermal frequency). These spatially dependent eigensolutions (v_i) represent *modes for heat transfer* across the beam. The modal solutions, v_i, are referred to later in this section. Characteristic thermal eigenmodes represented in two dimensions are shown on the right in Figure 5. These modes represent a temperature distribution that varies as a sinusoid with space. The corresponding material constants used in all simulations are shown in Table 3.
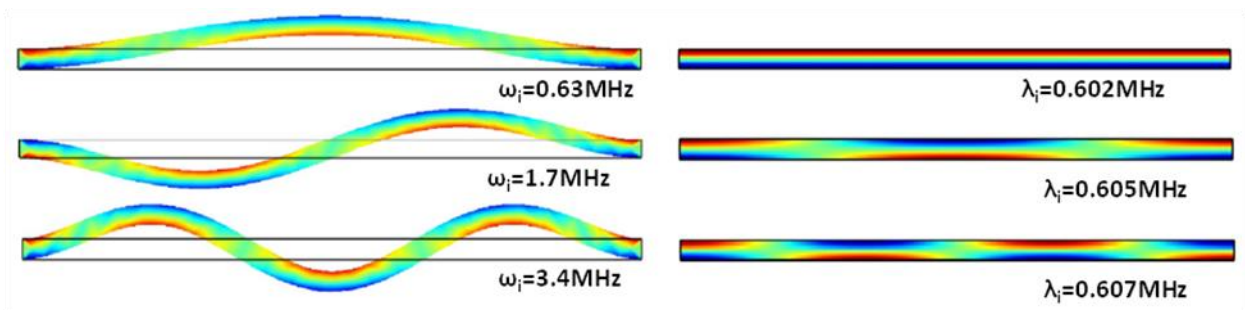
Figure 5: Uncoupled solutions of the mechanics and heat equations applied to a fixed-fixed beam 400µm by 12µm and a thickness of 20µm. Left: 2-D eigenmodes of the uncoupled mechanics equation. The color represents the axial strain in order to highlight regions of tension and compression. Red indicates compression and blue indicates tension. Right: 2-D eigenmodes of the uncoupled heat equation the color indicates temperature. The largest temperature gradients are areas that change from red (hot) to blue (cold).

Table 3: Material properties used for all simulations (figures: 4, 6, and 7)

2D Resonator	Units	Value
Material		polysilicon
Critical Dimensions	μm	400x12x20
Youngs modulus (E)	GPa	157
Density (ρ)	Kg/m^3	2330
Specific Heat (C_v)	$J/m^3 \cdot K$	1.63e6
Thermal Conductivity (κ)	$W/m \cdot K$	90
Thermal Expansion Coefficient (α)	ppm/K	2.6

Zener's Weakly-Coupled Approach

Zener originally developed general expressions for thermoelastic dissipation in vibrating structures.

Zener's early work shows his calculation methods based on fundamental thermodynamic expressions for

stored mechanical energy, work, and thermal energy that used coupled thermal-mechanical constitutive relations for stress, strain, entropy and temperature [28]. In order to compute these energy expressions for a specific resonator, Zener proposed that the strain and temperature solutions from the uncoupled dynamical equations (22 and 23) would be accurate. This approach assumes that the thermal-mechanical equations are only weakly-coupled. The thermoelastic quality factor for an isotropic homogenous resonator derived by Zener's technique is

$$Q^{-1} = \left(\frac{E\alpha^2 T_{init}}{C_v} \right) \sum_i \frac{\omega_{mech}\lambda_i}{\lambda_i^2 + \omega_{mech}^2} f_i = \sum_i f_i Q_i^{-1} \tag{25}$$

Where ω_{mech} is the mechanical resonant frequency and λ_i is the eigenfrequency of a given thermal mode. This equation shows how multiple thermal modes may add up to the damping of a single mechanical resonance. The contribution of a given mode, i, is determined by its weighting function f_i. This weighting function is determined by the effective coupling of the mechanical modes to the thermal domain (Figure 6).
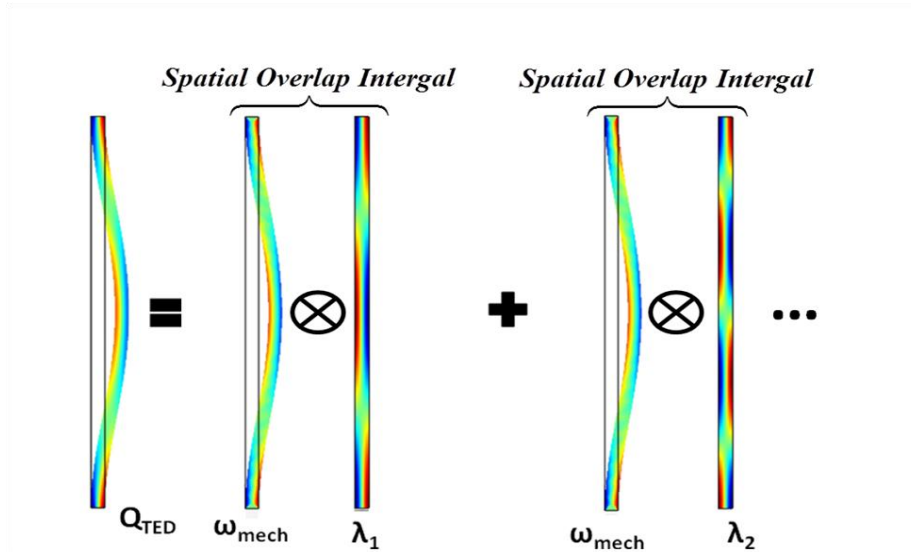
Figure 6: Thermoelastic damping can be calculated by summing the damping contribution of each thermal mode υ_i. Normalized strain profile is shown in the ω_{mech} resonance, and a temperature distribution is shown in the thermal mode resonances and overall Q_{TED} eigenvector. The damping contribution from each thermal mode is calculated by each mode's spatial overlap with the strain profile of ω_{mech} (represented by f_i in eq. 25).

Calculating the Weighting Function

The relative importance of each thermal mode, represented by the weighting function, f_i, in equation 25, depends on the spatial overlap between the mechanical mode and the thermal modes. The full derivation is presented in previous work [30], and the fundamental concepts are presented here. The rate of change of the volumetric strain ($\dot{\varepsilon}_1 + \dot{\varepsilon}_2 + \dot{\varepsilon}_3$) drives the source term in the coupled heat equation 18. For a general time harmonic steady state vibration, the source term, q, can be broken up into a spatial term and a temporal harmonic term

$$q = -\alpha(3\lambda + 2\mu)T_{init}(\dot{\varepsilon}_1 + \dot{\varepsilon}_2 + \dot{\varepsilon}_3) = -\alpha(3\lambda + 2\mu)T_{init}\frac{\partial}{\partial t}\varepsilon(x,y,z)\sin(\omega t) \tag{26}$$

The source term in equation 18 can now be written as

$$q = \underbrace{-\alpha(3\lambda + 2\mu)T_{init}\omega(\varepsilon(x,y,z)}_{spatial\ component} \times \underbrace{\cos(\omega t)}_{temporal\ component} \tag{27}$$

In order to solve equation 18, the spatial component of the heat source term, $(q(x,y,z))$, is projected on the thermal modes (v_i) of the system as

$$q(x,y,z) = \sum_i \alpha(3\lambda + 2\mu)T_{init}\omega a_i(v_i(x,y,z)) \tag{28}$$

where

$$a_i = \frac{\int_v \varepsilon(x,y,z)v_i(x,y,z)d\Omega}{\int_v v_i^2(x,y,z)d\Omega} \tag{29}$$

The magnitude of the overlap integrals, a_i, depends on the spatial overlap between strain at the resonance of the chosen mechanical mode and the corresponding thermal mode (v_i). A 2-dimensional

representation of this overlap is shown in Figure 7. Here the stress induced by mechanical resonance

provides a heat source to the various thermal modes. *The magnitude of heat transferred to each mode is*

dependent on how the stress profile maps to the thermal modes. Equation 29 describes this dependence.
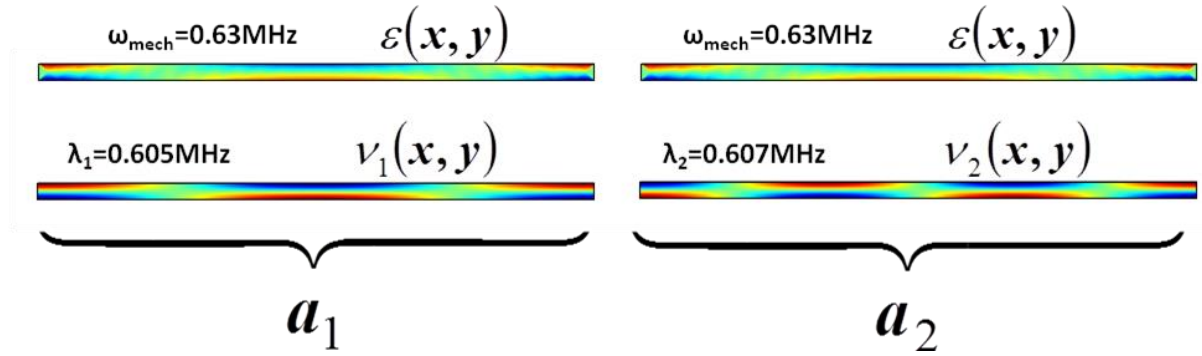
Figure 7: The overlap between the spatial distribution of strain represented by ω_{mech} and each thermal eigenmodes determines a_i. The larger the overlap, the larger the amount of heat transfer. In the above representation, a_1 has a larger value than a_2 because υ_1 has more spatial overlap with the strain, $\varepsilon(x,y)$, than υ_2. This is an important factor in determining which thermal mode will contribute most to TED in equation 26. The coloring in the thermal modes represents a temperature gradient and coloring on the mechanical modes represents the normalized strain profile. For our beam properties $a_1 \approx 5e-6$ and $a_2 \approx 9e-4$.

Using the source term (q) and an equation for temperature variation, an expression for entropy and energy

lost per radian W_{Lost} can be derived (see [30] for the derivation).

$$W_{Lost} = \frac{\pi(3\lambda + 2\mu)^2}{E} \sum_i a_i^2 \frac{\alpha^2 E T_{init}}{C_v} \frac{\omega \lambda_i}{\omega^2 + \lambda_i^2} \tag{30}$$

Now equation 30 can be substituted into equation 1 to obtain an equation for Q.

$$Q^{-1} = \frac{W_{Lost}}{2\pi W_{Stored}}$$

$$= \frac{(3\lambda + 2\mu)^2}{2EW_{Stored}} \sum_i a_i^2 \underbrace{\left(\frac{\alpha^2 E T_{init}}{c_v} \frac{\omega \lambda_i}{\omega^2 + \lambda_i^2} \right)}_{Zener's\ formula\ for\ Q_i^{-1}} \qquad (31)$$

This expression shows how Zener's formula for the coupling of each thermal mode in equation 26 relates to the overlap integrals (as represented by a_i) in equation 30. The energy stored in a resonator made of linear elastic material is given by

$$W_{Stored} = \varphi E \qquad (32)$$

where

$$\phi = \frac{(1-v)}{2(1-2v)(1+v)} \int_v \left\{ \left[\left(\frac{\partial u_1}{\partial x} \right)^2 + \left(\frac{\partial u_2}{\partial y} \right)^2 + \left(\frac{\partial u_3}{\partial z} \right)^2 \right] + \frac{2v}{1-v} \left(\frac{\partial u_1}{\partial x} \frac{\partial u_2}{\partial y} + \frac{\partial u_2}{\partial y} \frac{\partial u_3}{\partial z} + \frac{\partial u_3}{\partial z} \frac{\partial u_1}{\partial x} \right) \right\} dV \quad (33)$$

Here φ is the proportionality constant that relates the energy stored in a resonator and the elastic modulus. The value of this constant is determined by the displacement of the vibration equations and the constraint equation [30].

Now a simple expression can be written for the weighting coefficients by relating the Lamé parameters with Young's modulus and substituting equation 34 and 32 into equation 31, where v is Poisson's ratio.

$$(3\lambda + 2\mu)^2 = \frac{E^2}{(1-2v)^2}. \qquad (34)$$

Comparing this result with equation 25, f_i can be written explicitly.

$$f_i = \frac{1}{2}\frac{1}{\phi(1-2\nu)^2}a_i{}^2.$$

<div align="right">(35)</div>

Using Zener's approach: Thermomechanical Coupling

In order to use Zener's approach, the uncoupled heat (eq. 23) and mechanical (eq. 22) equations are solved, and the mechanical mode of interest is chosen. These equations can be solved by commercially available finite element solvers for any arbitrary geometry. The spatial overlap integrals, a_i, are computed along with the constant parameter φ (eq. 33). Equation 25 can then be used to calculate the total Q from adding all of the contributions for all significant thermal modes. Zener's weakly-coupled approach can give resonator designers insight into which thermal modes are the most significant and guidance on how to engineer around the thermoelastic damping by decoupling these modes. Contributions from the first 40 thermal modes in a 400 μm by 12 μm fixed-fixed thermally insulating beam are calculated by this method. The most significant thermal mode at 0.605MHz has a Q of 11,000 (Figure 8). The dominant thermal mode couples very strongly with the first mechanical mode. By placing 60 μm slots that block heat transfer in this dominant thermal mode the quality factor can be increased by a factor of 4.
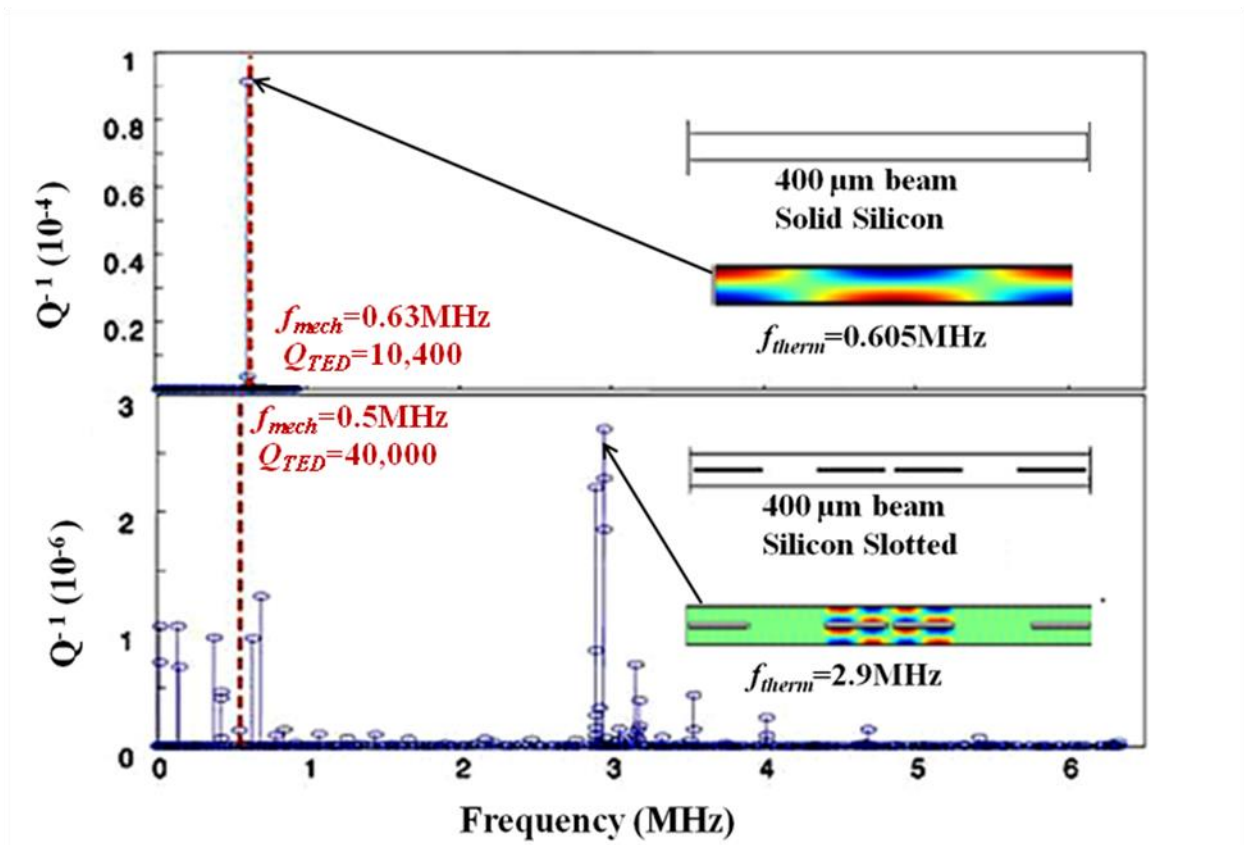
Figure 8: Q_i values for thermal modes in a fixed-fixed, thermally insulated beam 12 μm wide and 400 μm long. The x-axis is the frequency of each thermal mode λ_i, and the y-axis is $f_i Q_i^{-1}$ from equation 25. The contribution from each mode is then summed to give an overall Q_{TED} value. The top plot shows the solid beam thermal modes and mechanical resonance. One thermal mode at 0.63 MHz is the primary contributor to energy loss. The bottom plot shows the same beam with 1 μm x 60 μm slits along the beam length, where the energy loss from TED is decreased and distributed among many thermal eigenmodes. The dominant thermal modes are shown as inset plots. Both plots show the damping contribution from the *first 40 thermal eigenmodes*. Top: y-axis scale is 10^{-4} Bottom: y-axis scale 10^{-6}.

By suppressing the dominant thermal modes, designers are able to greatly improve quality factor. As shown in Figure 8, the slits effectively decouple the mechanical mode from the thermal mode at 0.605 MHz, and raise the **Q** from 10,400 to 40,000. It is worth noting that many additional modes are coupled in the design with slits, although the coupling is much weaker than the case of the solid beam.

Summary

This chapter presented two methods to evaluate and optimize N/MEMS structures for low thermoelastic damping. A derivation was given for the fully-coupled thermal-mechanical equations. Additionally, the weakly-coupled approach originally developed by Zener was reviewed, and a description of finite element based approaches to solve for TED in resonators with arbitrary geometry has been given. The weakly-coupled approach enables a great deal of insight into the energy loss mechanism. The spatial overlap between the strain profile of the mechanical mode and the temperature profile of the thermal modes has been shown to be a key factor in calculating thermoelastic dissipation. The technique of overlap integrals allows engineers to optimize geometries by decreasing the spatial overlap between the thermal and mechanical modes in order to significantly increase the quality factor.

Chapter 3 Anchor Loss

Introduction

The physical concept describing clamping loss is relatively simple. Clamping loss is caused by acoustic waves propagating in the substrate that carry energy away from the resonator. These waves are generated by the forces at the region of clamping, caused by the resonator's harmonic motion. Despite the relatively simple concept, clamping loss models in low frequency devices to date lack sufficient experimental verification.   Fabrication inconsistencies and fabrication-induced stresses are possibly causing the current conflicting experimental results. Our modified anchor loss model identifies intrinsic stress as a critical variable that may provide a previously missing link enabling the accuracy of this approach.

In order to gain a fundamental understanding of how anchor loss can be modeled it is useful to review how damping can be modeled mathematically. Generally we use a lumped element model to describe damping such as the viscous model (Figure 9). In the common viscous model damping is described as a force that is proportional to velocity. However damping can equivalently be described using an anelastic model which models the loss as a complex spring constant. The two models are equivalent as we can define damping constant c to be proportional to K and inversely proportional to ω. The anelastic damping model is especially useful to describe the phase relationship between x and F_s. This relationship is important so we can accurately describe the phase relationship between v and F_s which will determine our anchor loss using this direct modeling approach.

Viscous Damping Model

$$F_s = Kx$$

Equivalent

If $c = \dfrac{K\varphi}{\omega}$

and $\varphi \ll 1$

$$m\ddot{x} + c\dot{x} + Kx = F_a(t)$$

Anelastic Spring Model (Internal Friction)

$$F_s = K^* x = F_s e^{i\omega t}$$
$$x = x_o e^{i(\omega t - \varphi)}$$

$$m\ddot{x} + K^* x = F_a(t)$$
$$m\ddot{x} + K(1 + i\tan\varphi) = F_a(t)$$

φ is the loss angle by which x lags behind F_s
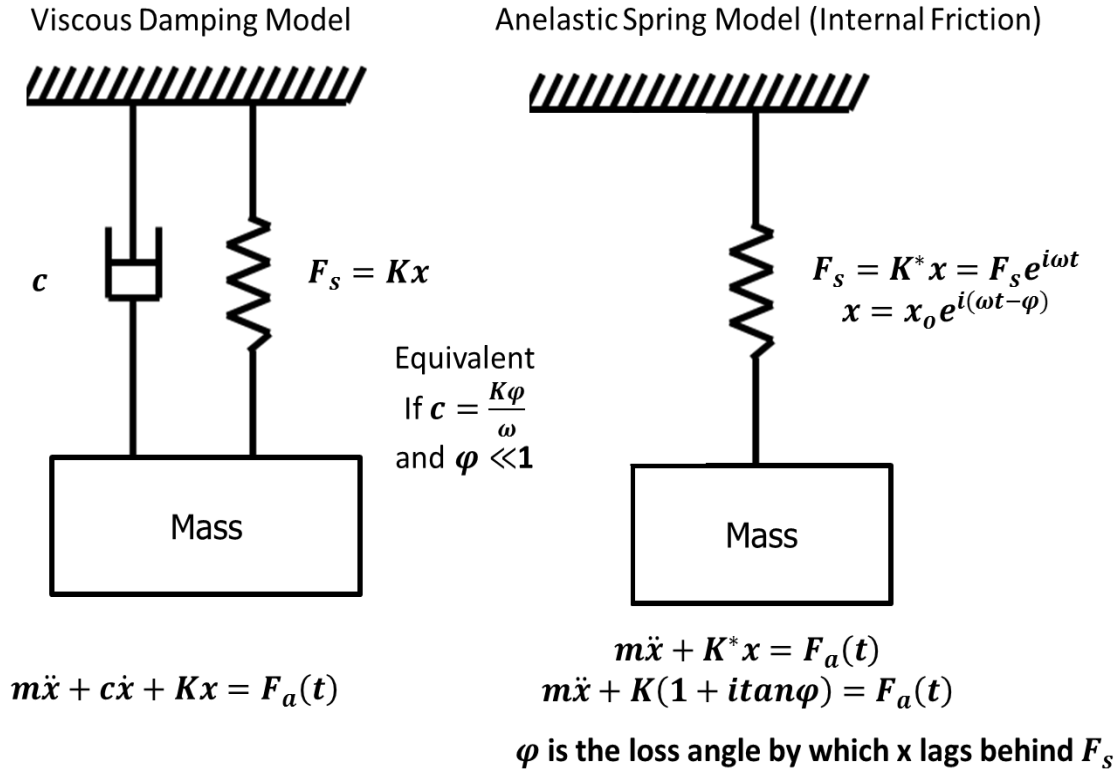
Figure 9: Anelastic damping model Vs Viscous damping. Damping in the anelastic model is described by a lag between the displacement *x*, and the restoring force, F_s .Both are mathematically equivalent however the anelastic model is useful to show how dissipation can change the phase relationship between F_s, *x* and *v*.

Motivation

Over the past two decades, high performance MEMS gyroscopes have been developed and successfully deployed in many military and commercial applications, including aeronautics and ballistics. While these MEMS gyroscopes have been very successful, the performance of these gyroscopes is still significantly inferior to the larger macroscopic gyroscopes. Many of these MEMs gyroscopes are operated at low frequencies and there is strong experimental evidence that suggests clamping loss is causing this performance degradation [31].

Current Method

The current approach to modeling anchor damping involves the use of a perfectly matched layer (PML) [32] to make the problem tractable when using the finite element method. The PML method makes the assumption that all energy that reaches the PML is irrecoverably lost (Figure 10). In order to

keep the simulation volume small enough to make finite element simulations tractable, the PML is placed within the thickness of a wafer. The PML assumption is valid at high frequency (100s MHz) devices because the acoustic wavelength is small. For low frequency devices however, the acoustic wavelength of the resonator is greater than the thickness of the wafer. As such, the PML may not accurately model the energy loss because energy that reaches the PML may not actually be lost. This inaccurate assumption is likely the reason that current clamping models can only capture general trends of Q but are not generally accurate. The work proposed here is to create and verify quantitatively accurate Q models for clamping.
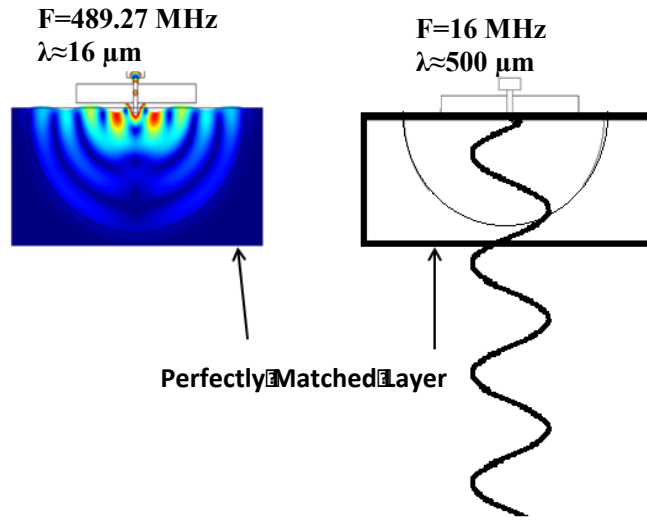
Figure 10: (left) COMSOL simulation showing that perfectly matched layer is sufficient for high frequency devices, whereas (right) perfectly matched layer is insufficient for low frequency devices because the wavelength is larger than the substrate thickness.

Proposed 3D Method

In order to model clamping loss, an intuitive modeling approach is adopted that involves calculating the stress and velocity fields at the anchor point and calculating the power loss per cycle. From the ratio of this power loss to the stored energy in the resonator, the quality factor can be calculated using the following equations:

$$Q_{Anchor} = \frac{\omega U}{\Pi} \tag{36}$$

23

$$\Pi = \iint_{S} \frac{1}{2} \operatorname{Re}\left(-\sigma_{ij} v_j{}^*\right) \tag{37}$$

$$U = \frac{1}{2} \iiint_{V} \{\sigma\}^{T} \{\varepsilon\} \tag{38}$$

Where Q_{Anchor} is the anchor limited quality factor, U is strain energy stored in the resonator, Π is the average power lost to the substrate, σ is stress, ε is strain and v is the velocity field at the anchor attachment point.

This approach is general and is directly related to a power calculation based on the force and velocity at the anchor point. The resonator dynamics are modeled utilizing a frequency response function, which is forced by a harmonic boundary load representing the actuation force (Figure 11). The high mesh density and accurate material parameters are crucial to obtaining accurate results with this approach. Intrinsic stress is included in the model as the calculated clamping loss and the resulting quality factor is highly dependent on this value. Q_{Anchor} can vary by orders of magnitude with changes in intrinsic stress, so knowledge of this parameter is critical to calculate accurate results. The full physics behind this modeling result still remains to be determined. In simulation, this intrinsic stress amplifies the anelastic loss term within the stiffness matrix C of the governing equation.

For our resonators, a value of 0.3 MPa compressive stress was estimated from knowledge of the fabrication process. The fabrication process used in this investigation is described in Chapter 5. In order for the solution to converge, a damping term is included. The damping term is based on TED, the only other relevant damping mechanism in the experimental devices used in this work. TED is also modeled using the Comsol multiphysics package.

In order to experimentally validate this model, ring resonators were fabricated using the Stanford vacuum epi-seal process [33]. The anchor structure design parallels the anchor structures of experimental gyroscopes, which often utilize a wine glass resonator mode attached to the substrate with a center post. Rings were scaled with various diameters in order to validate our modeling approach across a wide frequency range (200 kHz – 13 MHz) Figure 11 [34].
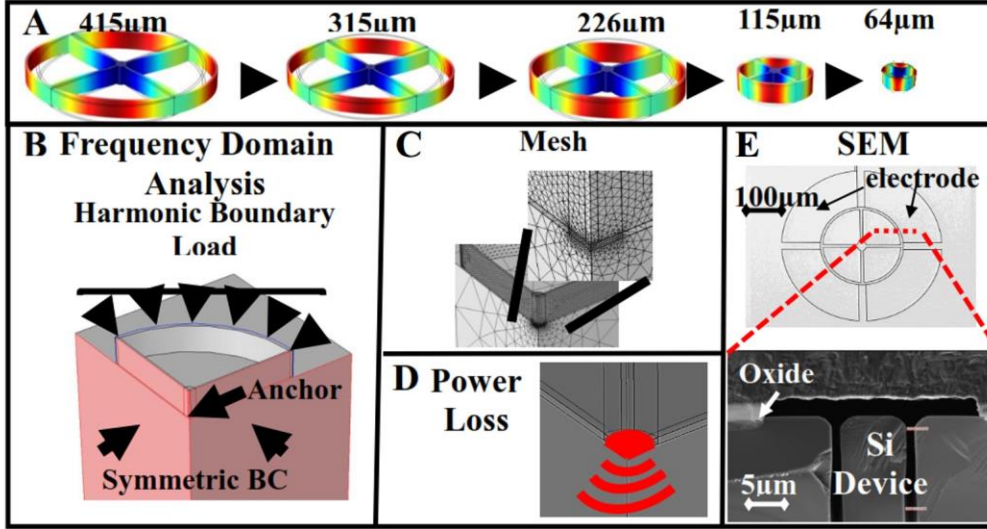
Figure 11: A) Scaled wineglass ring resonators. B) Frequency response model utilizing a boundary load and quarter symmetry C) Mesh distribution. High density mesh required at anchor point. D) Power loss is modeled by calculating the stress and velocity distribution at the anchor point. E) SEM pictures of the top of a 226 μm ring and a cross-section of the same device.

Advanced Theoretical Analysis

Upon analyzing equation 37, it becomes clear that for an undamped resonator the stress field at the anchor point will always be 90 degrees out of phase with the velocity and equation 37 representing anchor loss is zero. However, considering the full 3D governing equation with damping included as φ (Equation 39) the damping present at the anchor surface changes the phase relationship between F_s and v. Equation 40 shows how the dissipation ϕ is incorporated into the stiffness matrix C it can be seen that damping in the anelastic formulation [34] (Figure 9) will cause a phase shift and the stress field and the velocity to no longer be out of phase by 90 degrees and equation 37 (i.e. anchor loss) will become nonzero.

$$-\overbrace{\rho\omega u}^{Inertial} - \overbrace{\nabla\cdot\sigma}^{Re\,storing} = \overbrace{F_v e^{j\phi}}^{Input} \tag{39}$$

$$\sigma = \begin{bmatrix} C_{11}+i\phi & C_{12} & C_{13} \\ C_{21} & C_{22}+i\phi & C_{23} \\ C_{31} & C_{32} & C_{33}+i\phi \end{bmatrix}\cdot\varepsilon \tag{40}$$

The phase lag φ is directly related to the dissipation ($Q_{Internal}$) at that point in the resonator Figure 12. This relation is valid at each local element where dissipation is present.
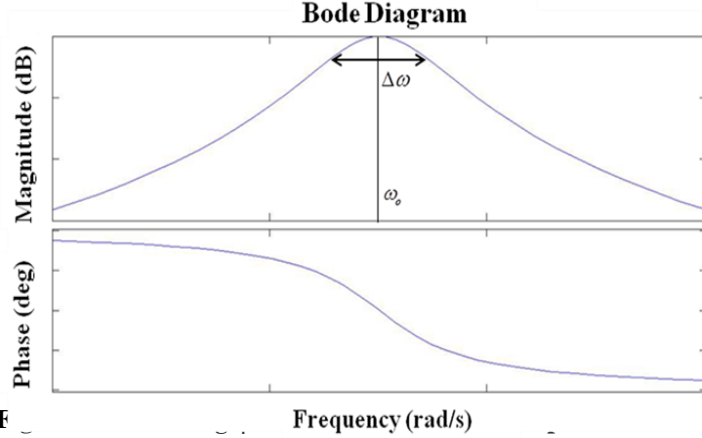
If $\varphi \ll 1$

$$\omega = \omega_r = \sqrt{\frac{K}{m}}$$

$$\frac{\omega_2 - \omega_1}{\omega_r} \overset{\text{def}}{=} \frac{1}{Q_{internal}} = \varphi$$

F... Frequency (rad/s) **...al phase offset between σ and v. This provides a theoretical explanation for why anchor loss is nonzero. From equation 37.**

Now if we consider a simple harmonic oscillator, we can use the anelastic damping formulation (i.e., a complex spring constant). First we define F_S, x and v.

$$F_S = K^* x = K(1 + \varphi i)x = |F_S| e^{i\omega t} \tag{39}$$

$$x = x_o e^{i(\omega t - \varphi)} \tag{40}$$

$$v = \dot{x} = v_o e^{i(\omega t - \varphi + \frac{\pi}{2})} \tag{41}$$

$$v^* = v_o e^{i(-\omega t + \varphi - \frac{\pi}{2})} \tag{42}$$

Now revisiting equation **37**,

$$\Pi = \iint_S \frac{1}{2} \mathrm{Re}\left(-\sigma_{ij} v_j^*\right) = -|\sigma_{ij}||v_j| \cos\theta \tag{43}$$

$$\theta = \varphi - \frac{\pi}{2} \quad for \varphi << 1 \tag{44}$$

$$\varphi = \frac{1}{Q_{Internal}} \qquad \theta = \frac{1}{Q_{Internal}} - \frac{\pi}{2} \tag{45}$$

26

$$\Pi = -\left|\sigma_{ij}\right|\left\|v_j\right\|\left|\frac{1}{Q_{Internal}}\right| \tag{46}$$

Given these relations an overall expression for Q can be reformulated assuming only anchor, TED and Akhieser is present. This simplification is used here as these internal dissipation mechanisms can be easily defined at the anchor surface .

$$\frac{1}{Q_{Total}} = \frac{1}{Q_{Anchor}} + \frac{1}{Q_{TED}} + \frac{1}{Q_{Akhieser}} \tag{47}$$

$$\frac{1}{Q_{Total}} = \frac{\left|F_s\right|\left\|v_o\right\|\left|\frac{1}{Q_{Internal}}\right|}{\omega U} + \overbrace{\frac{1}{Q_{TED}} + \frac{1}{Q_{Akhieser}}}^{Q_{Internal}} \tag{48}$$

$$\frac{1}{Q_{Total}} = \alpha_{Anchor}\left(\frac{1}{Q_{TED}} + \frac{1}{Q_{Akhieser}}\right) \tag{49}$$

$$\alpha_{Anchor} = \frac{\left|F_s\right|\left|v_o\right|}{\omega U} + 1 \tag{50}$$

This theoretical analysis presents a plausibility argument for how clamping loss could actually be an effect that magnifies other energy dissipation mechanisms, rather than a standalone mechanism itself. While this hypothesis is not fully proven, results in Chapter 8 will discuss some experimental evidence for this theory exploring the temperature dependence of anchor loss, where prior theories assert no temperature dependence for anchor loss.

Chapter 4 Optimization

Introduction

Historically MEMS device design has been limited primarily by available fabrication technologies, such as the achievable layer thickness for a given material stress or the minimum feature sizes that can be patterned. However, since MEMS research first began in earnest in 1982 [35] advancements in reliable, high aspect ratio [36] fabrication processes has allowed an ever increasing design space. For an increasing number of MEMS devices, there are opportunities to leverage design optimization as a low cost alternative to improve device performance within current MEMS fabrication processes. The increasing accuracy of modern multiphysics simulations [37,38] allows device performance in many cases can be predicted a priori. Through accurate simulation and design optimization, MEMS designers can improve device performance while saving time and costs by not relying on trial and error. This savings is achievable by decreasing the number of fabrication runs.

Background

The rapidly expanding field of design optimization has interesting theoretical implications as well as practical relevance in manufacturing and innovative design. Two distinct approaches to optimization have become prevalent, gradient based optimization schemes and non-gradient based optimization methods. The more traditional optimization schemes can be classified as gradient-based optimization. These include the density SIMP approach [39], the level set approach [40], and the method of moving asymptotes (MMA) [41]. All of these methods rely on calculating the gradient of the objective function along different search directions. In many problems, such as structural topology and heat transfer, these techniques are effective and efficient and are the ideal choice for optimization method. However, these methods are not as computationally efficient in non-self-adjoint and non-symmetric systems where

significant computational effort is required to calculate gradients in each search direction and when the objective function is non-smooth. For these systems, non-gradient based approaches are often effective. Non-gradient-based optimization includes genetic algorithms (GAs) [42], ant colonies [43], simulated annealing [44] and particle swarm optimization [45]. These methods have been recently developed and have proven effective in many complex multidimensional problems.

Optimization for Low TED Resonators

For the specific investigation of optimizing TED, a particle swarm optimization was the method of choice. The particle swarm optimization was chosen for several reasons. First, the complex coupled physics involved in calculating TED form a non-self-adjoint, non-symmetric system where gradient-based optimization methods are more difficult to implement because the gradient is not continuous in every direction. . Also, the particle swarm optimization has all candidate designs available at the beginning of each iteration, which opens the possibility of parallel computation, a feature recently added to commercial multiphysics finite element software. In addition, particle swarm optimization has the advantage of very few tunable parameters when compared to other non-gradient-based approaches (GAs, simulated annealing etc), which, simplifies the process of tuning convergence.

Intuitive Low TED Design Approach

A standard intuitive design approach has previously been applied to beams in an effort to minimize TED [46]. This approach used the fully coupled thermoelastic governing equations and FEM to simulate thermoelastic dissipation in a beam resonating in the first mechanical mode. The optimization consisted of varying the position of two slits in order to determine the optimal location to reduce thermoelastic dissipation (Figure 13). The governing equations for TED form a coupled PDE. These coupled PDEs are solved as an eigenvalue problem, with the coupled equations shown in Table 2. The eigensolutions of these coupled PDEs result in a complex eigenfrequency where the imaginary part of the eigenfrequency determines the damped resonant frequency, and the real part represents the relative thermoelastic loss. This coupled-simulation method has been verified with experimental results [46] and is leveraged in this work as part of the design optimization process. The material properties used in simulations can be found in Table 3.
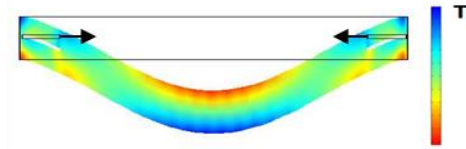
Figure 13: Previous state of the art intuitive design approach, where open slots are placed in the beam to affect TED. The temperature gradient across beam is shown. Numerical temperature is not shown because the magnitude of the temperature depends on the forcing function, which is not included in this eigenvalue analysis. This is a 12 µm by 400 µm clamped-clamped silicon beam. The position of the 1 µm by 40 µm slot was varied along the beam in search of a high quality factor. A *Q* value of 17,600 was achieved with the slot edge 2 µm from the anchor, as compared to a minimum *Q* of ~10,000 for a solid beam.

Particle Swarm Optimization

A common analogy used to conceptualize the optimization technique is to compare it to a swarm of bees (agents) searching a 2D field for the position with the highest concentration of flowers (Figure 14). The percent concentration of flowers represents the *fitness value* (Q limited by thermoelastic dissipation, Q_{TED}) at each location. Each bee remembers only the location of its own personal best and the location of

the global best concentration of flowers that has been investigated by the swarm. At each time step, the

velocity of each bee is altered to steer it toward its own personal best and toward the location of the global

best of the entire swarm. The bees should eventually converge on the highest concentration of flowers in

the field. A key aspect of this technique is that a very large design space can be efficiently searched,

resulting in a solution that, while not mathematically guaranteed to be the global optimum, tends to

approach this optimum.
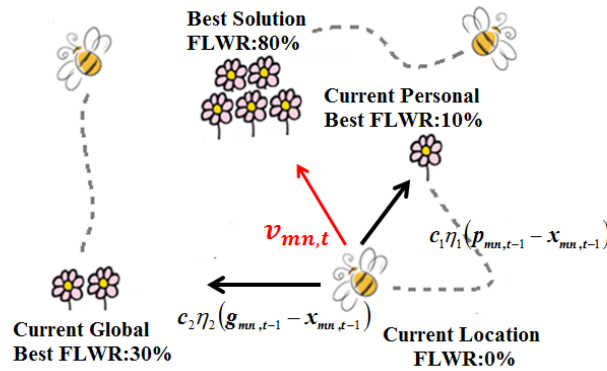
Figure 14: Swarm of bees (*agents*) searching a 2D field to find the location of the highest concentration of flowers. Each bee is accelerated to its own personal best and global best of the swarm characterized by the highest flower concentration (FLWR). Adapted from [46].

Binary BPSO

A binary implementation of PSO is used in this investigation. Binary Particle Swarm Optimization

(BPSO) is used because the size of the smallest element in the resonator is tunable, and the nature of

BPSO permits a wide variety of designs, including non-intuitive ones, to be explored. BPSO formulates

each design as a binary string that represents the presence or absence of material, where the length of the

string is equal to the number of elements in the design space. For example a 12 μm x 400 μm beam shape

(in 2-D, extruded into the third dimension) with 4 μm x 4 μm elements would have a total of 300

elements, where each element could either represent material or absence of material. The design space is

therefore all possible binary combinations of the string. Velocity in BPSO becomes the probability that

an element of the design will be present or absent. A concise explanation of the BPSO is available in previous work [47]. The equations used for updating velocity in binary space are described below.

The binary matrix $X_{mn,t-1}$ contains the variables defining the nth pixel of the mth agent's design at iteration t-1, equation (51).

$$\{x_{mn,t-1}\} = \{x_{m1,t-1}, x_{m2,t-1}, \ldots x_{mN,t-1}\}$$
$$x_{mn,t-1} \in \{0,1\}$$

(51)

The velocity is updated according to equation (52)

$$v_{mn,t} = v_{mn,t-1} + c_1 \eta_1 (p_{mn,t-1} - x_{mn,t-1})$$
$$+ c_2 \eta_2 (g_{mn,t-1} - x_{mn,t-1})$$

(52)

In the above equation, c_1 and c_2 are tunable weighting coefficients that determine the relative importance of the global best and the personal best, respectively. In this investigation we set c_1 and c_2 to 1. These weightings were experimentally determined to allow for adequate local exploration while also ensuring convergence in under 200 iterations. Convergence was defined in this case as occurring when the standard deviation of the objective value of the 20 agents falls within 6% of the current global optimum. This convergence criteria is chosen to provide reasonable convergence time while exploring a reasonable design space. A smaller standard deviation is difficult since inherently there is ~1% variance in the calculated Q_{TED}, even when the same design is simulated twice. η_1 and η_2 are random variables (0-1) computed at each time step to increase variability. There are two acceleration terms in this equation: one pulls the current bit n toward the global best value, ($g_{mn,t-1}$), while the other pulls the current bit to the personal best ($p_{mn,t-1}$). The possible values for each term are 1, 0, -1 as shown in equation 53.

$$p_{mn,t-1} - x_{mn,t-1} = \begin{cases} 1; p_{mn,t-1} = 1, x_{mn,t-1} = 0 \\ 0; p_{mn,t-1} = x_{mn,t-1} = 0 \\ 0; p_{mn,t-1} = x_{mn,t-1} = 1 \\ -1; p_{mn,t-1} = 0, x_{mn,t-1} = 1 \end{cases}$$

(53)

In (2), an increase in $v_{mn,t}$ increases the probability of the nth bit becoming 1, while a decrease in $v_{mn,t}$ decreases this probability. Equation 54 converts the real valued $v_{mn,t}$ to a sigmoidal function $S(v_{mn,t})$ that is compared with a random number $r_{mn,t}(0\text{-}1)$, generated at each time step for each bit, in order to determine the actual value of $X_{mn,t}$ at each time step.

$$S(v_{mn,t}) = \frac{1}{1+e^{-v_{mn,t}}} \qquad x_{mn,t} = \begin{cases} 1 \; if \; r_{mn,t} < S(v_{mn,t}) \\ 0 \; if \; r_{mn,t} \geq S(v_{mn,t}) \end{cases} \qquad \textbf{(54)}$$

Binary BPSO Applied to Resonator Design

In order to apply BPSO to resonator design, a binary matrix of specified dimensions is mapped to a beam geometry for TED analysis in COMSOL® (Figure 15). The optimization was computed in Matlab and interfaced with the COMSOL® simulation for the *fitness value* (Q_{TED}) calculation. The beam dimensions are set to 12 μm by 400 μm and beam half symmetry is used to reduce the computation time. The size of each binary pixel is set to 10 μm by 2 μm in the low-resolution optimization and is set to 2.5 μm by 1.71 μm in the high-resolution optimization.

A lower limit of 0.5 MHz was applied in order to restrict the optimization in the frequency domain. This limit was introduced because as material is removed the effective width of the resonator is decreased and the frequency drops. It is straightforward to design a high Q_{TED} resonator at very low frequency, the novelty in this approach is to optimize Q_{TED} at an arbitrary frequency. A fitness value of 0 was assigned to any resonator design that fell below this value. This restriction allows resonator designers to choose a desired resonant frequency and optimize Q_{TED} at that frequency.

In addition to these design constraints, checkerboard designs, (two diagonally adjacent solid bits) were thrown out by restarting the stochastic design selection when a checkerboard design was encountered. These designs result in singularities, which cause simulation errors. Additionally, the corner connections would be very difficult to fabricate.
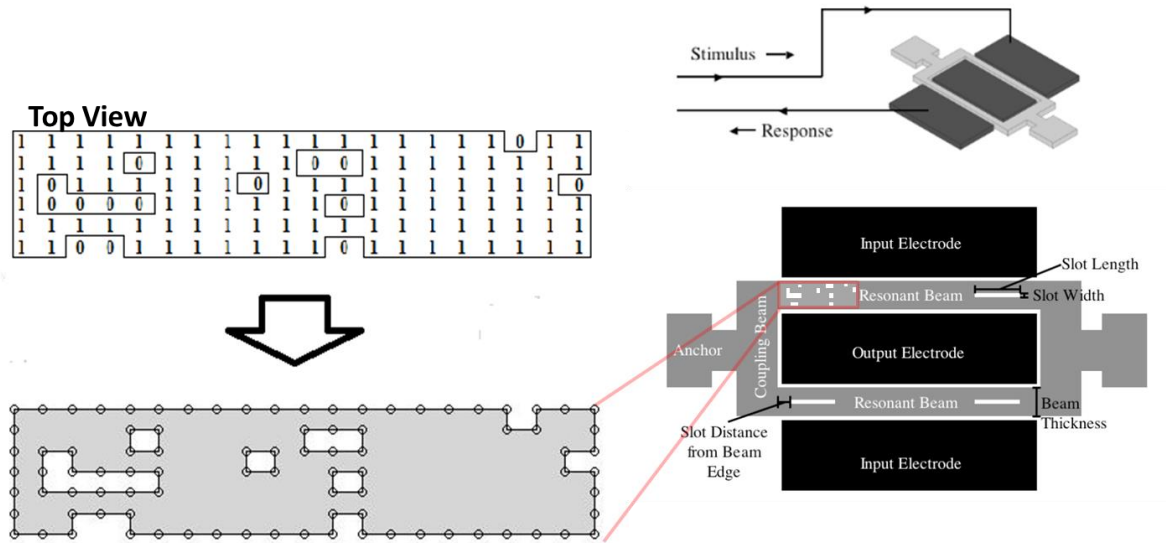
Figure 15: BPSO binary mapping translated to tuning fork resonator design.

Simulation Results

Two separate trial were simulated to test the effectiveness of the BPSO algorithm. First, The "BPSO Low Res" was performed for three trials, with each trial comprising 150 iterations of 20 agents (Figure 16). The "BPSO low Res" consists of a 400x12x20 μm resonator composed of 10x2 μm bits. Random starting locations were generated, and the same starting locations were used for each trial. An optimized geometry with a Q_{TED} of 43,000 was established ("BPSO Low Res"). Experimental results will be needed to confirm there is no influence from other loss mechanisms that cannot at present be accurately modeled. The optimum Q_{TED} of 43,000 was only a slight improvement over the best intuitive design. The best intuitive design was also used as a starting location in an additional low-resolution optimization in order to explore the possibility of combined intuitive and algorithmic optimization. This additional optimization resulted in a slightly higher Q_{TED} of 45,000.
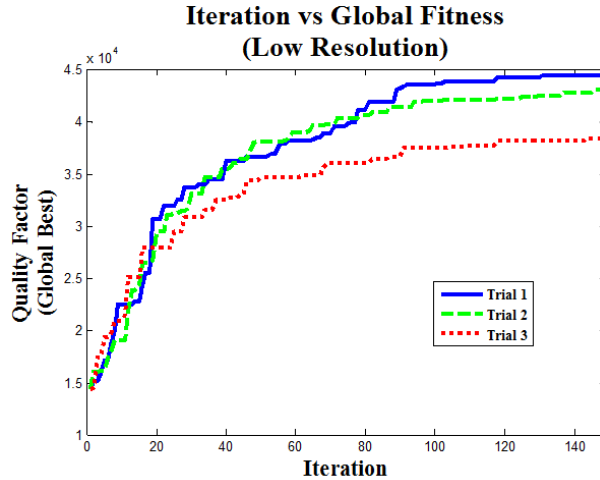
Figure 16: Iteration vs. global best quality factor. Three Optimization trials are shown with 20 agents run for 150 iterations with resolution of 10 μm by 2 μm. All trials are comparable to the best intuitive design. The best geometry achieves $Q \approx 43{,}000$. If we seed this optimization with the best intuitive design this optimization achieves $Q \approx 45{,}000$.

Next, a high-resolution optimization was performed with each bit set to 2.5 μm by 1.71 μm in an attempt to further increase Q_{TED}. This resolution was chosen because it is reasonably achievable by standard micromachining processes. The reduced bit size allowed much more freedom in the design. However with an extremely large solution space of 2^{560}, exploration is very computationally intensive.

The intuitive design was again used as a starting location to narrow the search, enabling intuition and design optimization to complement each other. This high resolution optimization was run for three trials with the best design achieving a Q_{TED} of 56,000, shown in Figure 17. The BPSO is able to find optimized solutions that achieve significant improvement in Q_{TED} with a relatively insignificant change in resonant frequency. All optimizations are compared in Figure 18. In order to increase Q_{TED} to 56,000 by scaling frequency of a solid beam of fixed width to avoid thermomechanical coupling, the frequency would need to be decreased from 0.5 MHz to below 50 KHz or increased to at least 6.5MHz. In order to achieve these frequencies with a solid beam, the width would need to be increased or decreased by over a factor of 10 to 1.2 μm or 120 μm which creates significant fabrication challenges due to either resolution limits or ability to release wide devices.

Iteration Vs. Global Fitness (High Resolution)
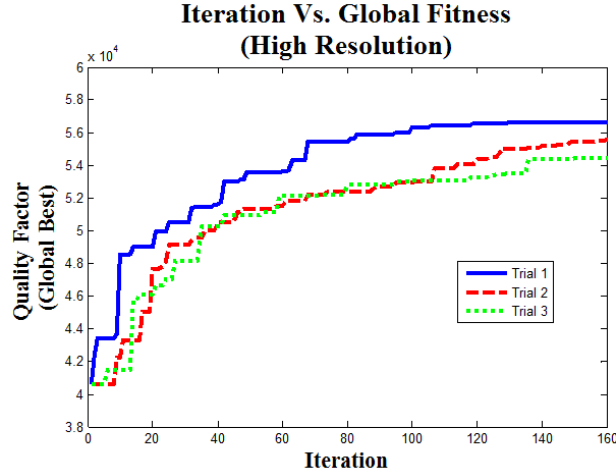
Figure 17: Iteration vs. global best quality factor for the high resolution optimization. Three optimization trials are shown, with each trial consisting of 20 agents run for 150 iterations with resolution of 2.5 μm by 1.7 μm. The best intuitive design is used as a starting location for one of the agents. This optimization increases Q_{TED} by 40% to 56,000.

BPSO Versus Intuitve Design
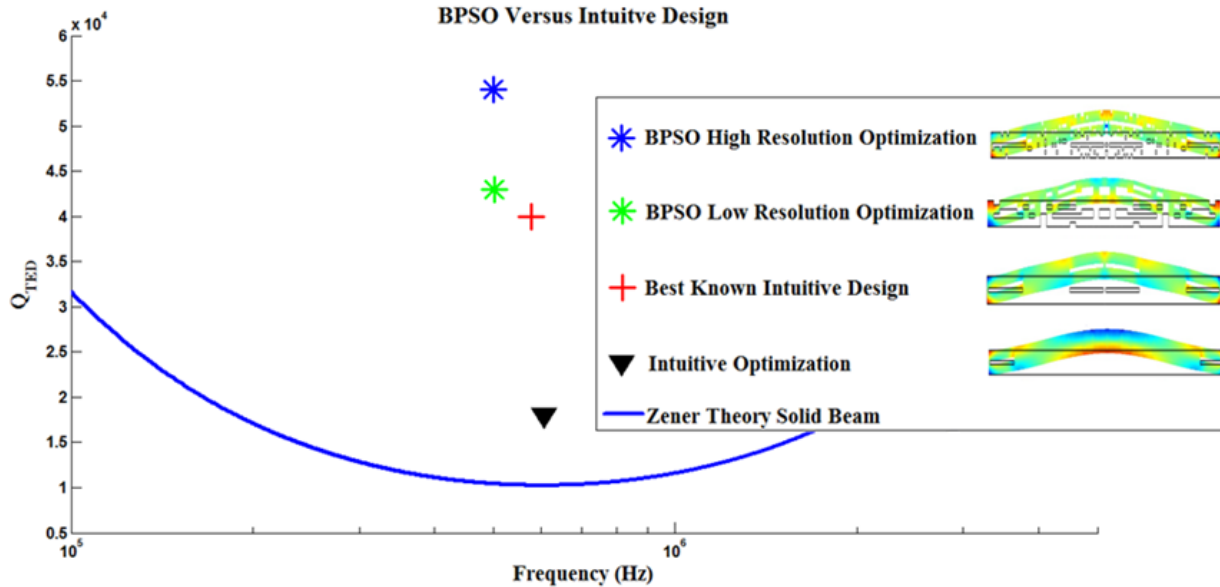
Figure 18: The simulated Q_{TED} using BPSO is 40% higher than the previous best intuitive design. The intuitive design involved parametrically sweeping the location of slots cut into the beam along the beam length [24]. The best known intuitive design followed the intuitive optimization by placing slots in regions of high thermal-mechanical coupling. Designs from BPSO optimization have decoupled areas with high strain from the beams various thermal eigenmodes resulting in a highly non-intuitive design.

36

Analysis of Optimized Thermal Eigenmodes

While the exact designs discovered by these initial optimizations have not been experimentally verified, the method for simulating TED has been confirmed through experiments [46]. The fully-coupled simulations provide very accurate Q_{TED}, however this method does not provide the same design insight as accomplished by a weakly coupled approach introduced in Chapter 2. Using this approach, the uncoupled thermal and mechanical equations are solved separately.

   Reintroducing from chapter 2, the damping of the beam can be estimated using the overlap integrals of each thermal eigenmode and the chosen mechanical eigenmode [29]. Zener derived a general expression for how each thermal mode contributes to the overall Q_{TED}

$$Q_{TED}^{-1} = \left(\frac{E\alpha^2 T_{init}}{C_v} \right) \sum_i \frac{\omega_{mech}\lambda_i}{\lambda_i^2 + \omega_{mech}^2} f_i = \sum f_i Q_i^{-1} \tag{25}$$

where ω_{mech} is the mechanical resonant frequency, λ_i is the eigenfrequency of each thermal mode. Q_i^{-1} is the damping contribution of each thermal mode in the case of maximum thermomechanical coupling. This equation shows how multiple thermal modes add together to the overall Q_{TED}. The relative importance of each thermal eigenmode can now be analyzed and our optimization can be compared with the intuitive design. As can be seen in Figure 19, the design optimization algorithm discovered a geometry that decouples the mechanical eigenmode and the thermal eigenmodes around 3.36 MHz, which dominate energy loss in the intuitive design. The exact sequence of holes also prevents the coupling between the other adjacent thermal modes and spatially decouples the strain gradient from the thermal modes. All thermal mode coupling has been suppressed except for two thermal modes that couple with stress at the anchor point.
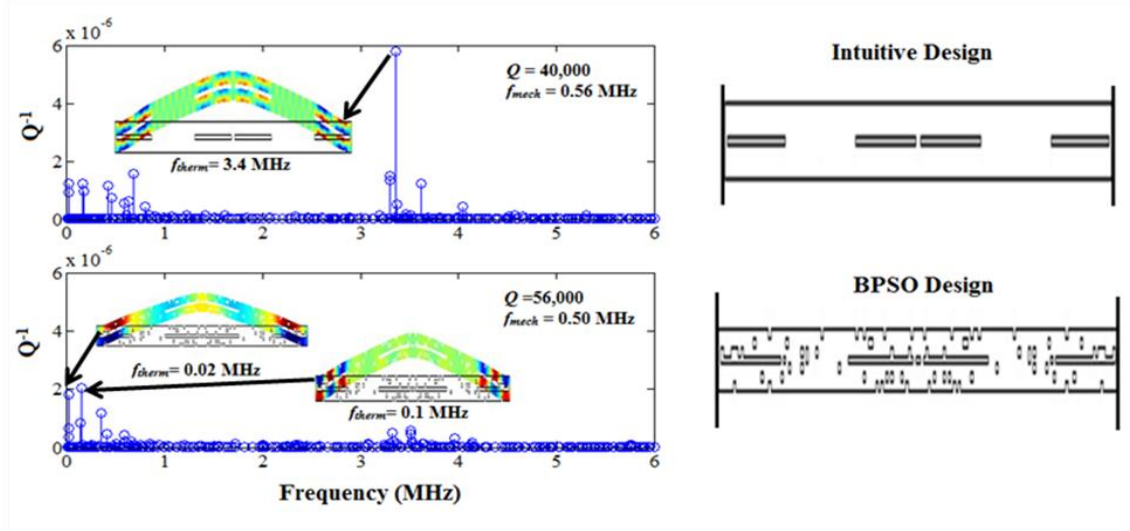
Figure 19: Comparison of the intuitive design approach (top) to the BPSO optimization (bottom) with low- and high-resolution optimizations. Thermal eigenmode stem plots are shown on the left, and resonator topologies are shown on the right. Stem plots show the contribution of each thermal eigenmode to _Q_, as determined by the weighting function in equation 7. _Q_ values are simulated for the first 400 thermal modes in a fixed-fixed thermally insulated beam of dimensions 400 μm by 12 μm. Inset plots show dominant thermal modes. The top plot shows the design before optimization and the bottom plot shows the same beam after BPSO optimization where all thermal mode coupling has been suppressed except for the coupling at the anchor point.

Disscussion

Intuitive Design Approach

Intuitive knowledge of TED has enabled slotted resonators to significantly decouple the thermal and mechanical eigenmodes and increase Q_{TED} as much as a factor of four when compared with a solid beam [29]. However, if this approach is repeated by manually trying to decouple the dominant thermal eigenmodes sequentially, the quality factor does not necessarily increase. In repeating the intuitive optimization, the remaining dominant thermal eigenmode can be effectively decoupled; however, the design changes will also affect the coupling of the other thermal eigenmodes. For example if we take the best intuitive design and place a hole directly blocking the heat flow of the dominant mode at 3.36MHz (Figure 20) Q_{TED} actually decreases slightly to 39,000. We can analyze this by using Zener's weakly coupled approach. It can be seen that the added holes effectively decouple the 3.36MHz thermal mode,

but new higher and lower frequency modes now contribute significantly to the damping and actually

lower the overall Q_{TED}.
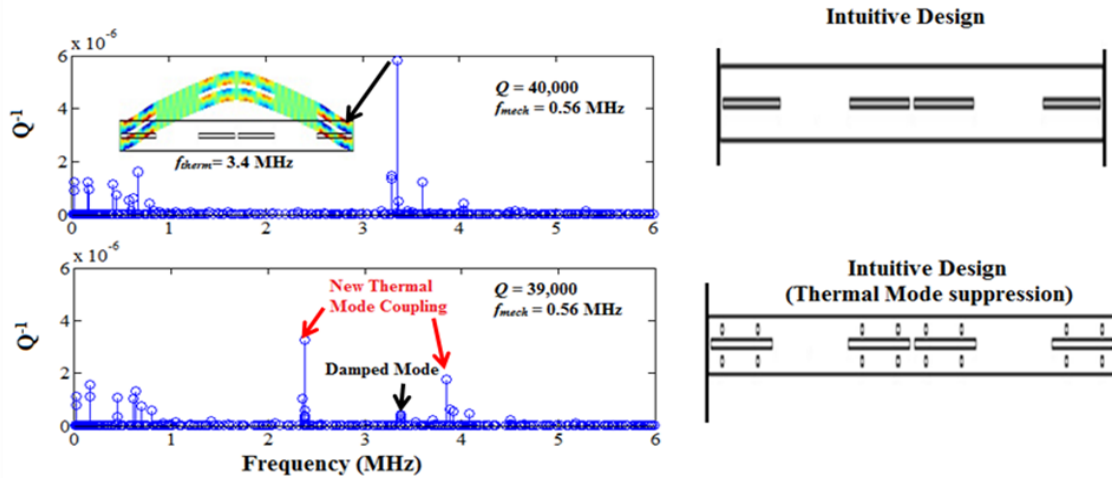
Figure 20: Zener's weakly coupled approach. The contribution from each thermal mode can be quantified and analyzed. It becomes increasingly complex to try to decouple each dominant thermal modes manually, since with each change in geometry the coupling of the other thermal modes to the mechanical mode will change as well which may lead to an increase or decrease in Q_{TED}. This example shows Q_{TED} degrades slightly when additional slots are added to "block" heat flow.

Method Evaluation

This method provides a significant improvement over the previous intuitive design approach and

actually works best in concert with the intuitive approach by using intuitive designs as starting locations

for the searches. While BPSO does not guarantee a global optimum, it does allow for significant

flexibility in the design space. This flexibility enables the optimizations to be tuned to match exact

manufacturing capabilities. As can be seen from the differences in the low resolution optimization and

the high resolution optimization, the optimized design and Q_{TED} are resolution dependent. The resolution

described here is the resolution selected for the BPSO elements, not the mesh density of the finite

elements; the meshing of these designs is fine enough that Q_{TED} is not dependent upon mesh size. The

resolution dependence is to be expected since the design space is much larger in the high resolution

optimization. Better exploration of the design space can be accomplished with parallelization or with a more efficient alternative method.

Conclusion

This work has introduced BPSO optimization of $\boldsymbol{Q_{TED}}$ in MEMS resonators, representing the first use of topological design optimization to minimize energy dissipation in MEMS. The complexity involved in solving the coupling between the structural and thermal domains makes optimization of $\boldsymbol{Q_{TED}}$ an ideal candidate for non-gradient based optimization. Simulations show optimized designs having a TED-limited Q 40% greater than previous state of the art without significantly affecting the mechanical resonant frequency. Due to the large solution space available, a variety of solutions can be used to maximize the quality factor. The flexibility of topological optimization enables discovery of non-intuitive designs and flexibility to dictate manufacturing resolution during the design process. As such, the BPSO technique has the potential to optimize many other N/MEMS devices due to its simplicity and versatility. Full experimental results with fabricated devices is presented in Chapter 7.

Chapter 5 Fabrication

Introduction

Design optimization is an interesting intellectual exercise in its own right. However, if designs cannot be reliably manufactured to meet this optimized performance the commercial application of this technique is limited. In this work we are focused on establishing an optimization technique that is flexible and results in fabrication ready design masks.

Historically, MEMS research has focused on improving the fabrication process for each device. Improvements in fabrication often result in an improvement in yield, reliability and performance. Different devices often have a unique process flow and unique design constraints. In this work, we are interested in leveraging simulation and optimization as opposed to improved fabrication capabilities to boost performance. We have a dual pursuit. First our goal is to develop a practical design optimization technique for high Q, low TED resonators. Secondly we aim to improve fundamental understanding and accurate modeling of MEMS resonator dissipation. In order to satisfy these goals we require a stable, high yield fabrication process, due to its many strengths the Stanford epi-seal process [48, 49] is used in this investigation.

Stanford Epi-seal MEMS

The epi-seal encapsulation process is a wafer-level encapsulation for silicon structures released and sealed in vacuum, without a surface coating of silicon dioxide, which is inherently present on devices exposed to the ambient. This efficient high yield process is currently being used at SiTime, a company focused on commercialization of silicon resonators for timing [50].

Epi-seal Process Flow

The epi-seal process is shown in Figure 21. The process proceeds as follows A) silicon on oxide (SOI) wafer is etched using Deep Reactive Ion Etching (DRIE) to define the device layer. B) A sacrificial oxide is deposited to fill the trenches and to be used as a top spacer layer. C) Contacts are etched in the oxide and a silicon layer is deposited in an epitaxial reactor. Epitaxial silicon is grown on any exposed device layer and polysilicon is deposited on any oxide surface. Subsequently vents are etched in this cap D) HF vapor is used to etch the oxide around the vents and release the device. A high temperature bake is used to remove native oxide and a second layer of epitaxial silicon is deposited to seal the device. E) Aluminum is then deposited to define the electrical contacts. The process has design rules as follows. A top view SEM of the device layer of a tuning fork resonator after the first DRIE (Step A) is shown in Figure 22[51].
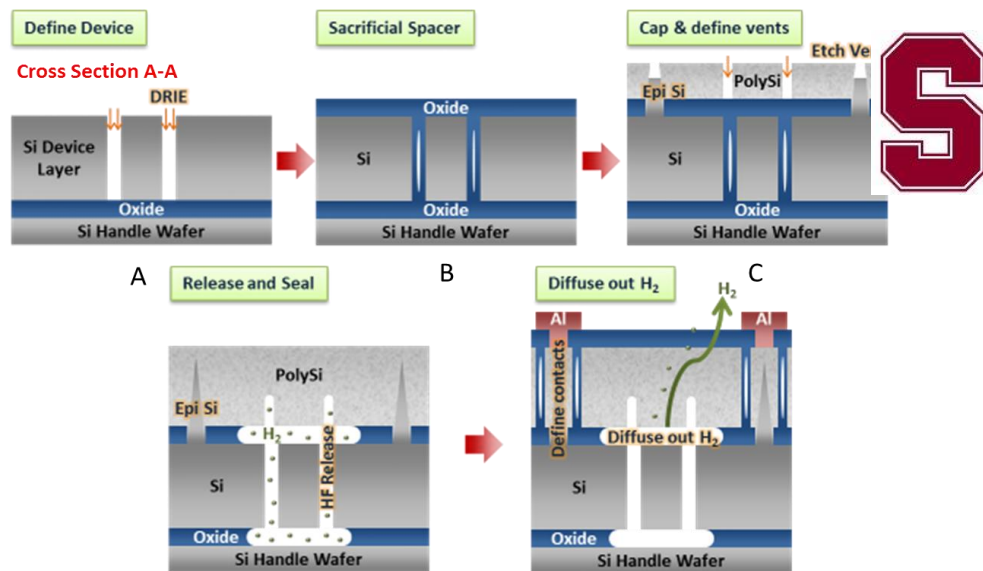
Figure 21: Epi-seal Fabrication sequence A) silicon on oxide (SOI) wafer is etched using Deep Reactive Ion Etching (DRIE) to define the device layer. B) A sacrificial oxide is deposited to fill the trenches and to be used as a top spacer layer. C) Contacts are etched in the oxide and a silicon layer is deposited in an epitaxial reactor. Epitaxial silicon is grown on any exposed device layer and polysilicon is deposited on any oxide surface. Subsequently vents are etched in this cap D) HF vapor is used to etch the oxide around the vents and release the device. A high temperature bake is used to remove native oxide and a second layer of epitaxial silicon is deposited to seal the device. E) Aluminum is then deposited to define the electrical contacts.

Figure 22 Step A: Top View SEM Optimized tuning fork resonator

Epi-seal Design Rules

The Epi-seal process design rules are shown in Table 4.

Table 4 Epi-seal Design Rules

Die space	2000 μm x 2000 μm
Device Thickness	40 μm
Device to Substrate	2 μm
Device to cap	2 μm
Maximum released area	450 μm x 450 μm
Trench width	0.7-1.5 μm
Min trench length	5 μm
Min dimension between trenches	3 μm
Max released feature dimension	12 μm
Min electrode dimension	100 μm
Min non released structure	40 μm

In order to incorporate the Epi-seal design rules into the binary particle swarm optimization explored in Chapter 4 it is necessary to identify prohibited designs and reject them by stochastically regenerating designs until the design meets all requirements. This is accomplished by the error checking code (shown in appendix i). The bit dimensions and prohibited designs shown in Figure 23.

Prohibited Designs
(Top View)

No corners

No Vertically Adjacent 0s

No Auxiliary Resonances
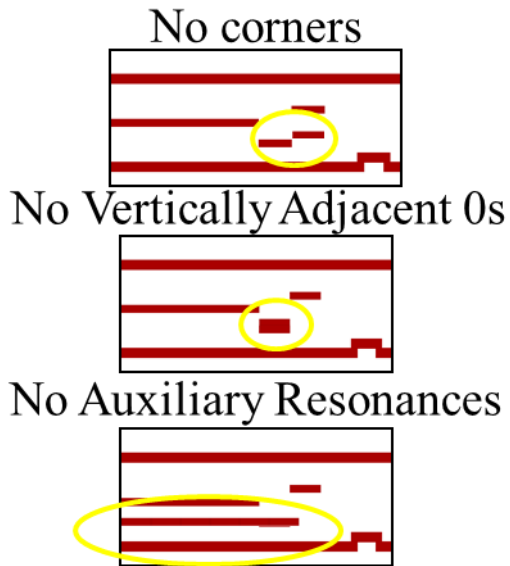
Minimum Dimensions

5μm

↕ 1.5μm
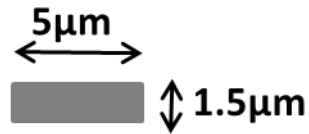
Figure 23: Design Restrictions due to Fabrication Process and minimum slot dimensions. Corners result in unstable designs. Two vertically adjacent slots result in a trench that is too wide for the design rules and no structures which result in unwanted auxiliary resonances.

Conclusions

Stanford's Epi-seal fabrication process provides an ideal MEMS process flow for investigating limiting fundamental mechanisms. The process provides a stable, consistent and clean environment, which greatly reduces fabrication induced performance degradation [52]. The process also provides vacuum sealed devices that reduce introduction of contaminants and greatly simplifies device testing (a vacuum chamber is not required to remove air damping for testing). The epi-seal design rules are incorporated into the optimization scheme described in chapter 4 and the optimization algorithm outputs fabrication ready structure design masks.

Chapter 6 Experimental Study Design

Two distinct experimental studies were performed using the epi-seal process. The objective of the first study was to investigate the use of a binary particle swarm optimization to optimize resonators with low TED. The objective of the second study was to investigate clamping loss with the goal of developing an accurate general 3D anchor loss model.

Study Design:Thermoelastic Optimization

With the Epi-seal design rules incorporated into the binary particle swarm optimization, a final optimization was performed that prohibited designs in Figure 23 and utilized design rules from Table 4. The convergence plot from this optimization is shown in Figure 24. This Plot shows how the BPSO algorithm performed when the epi-seal design rules were integrated into the algorithm.
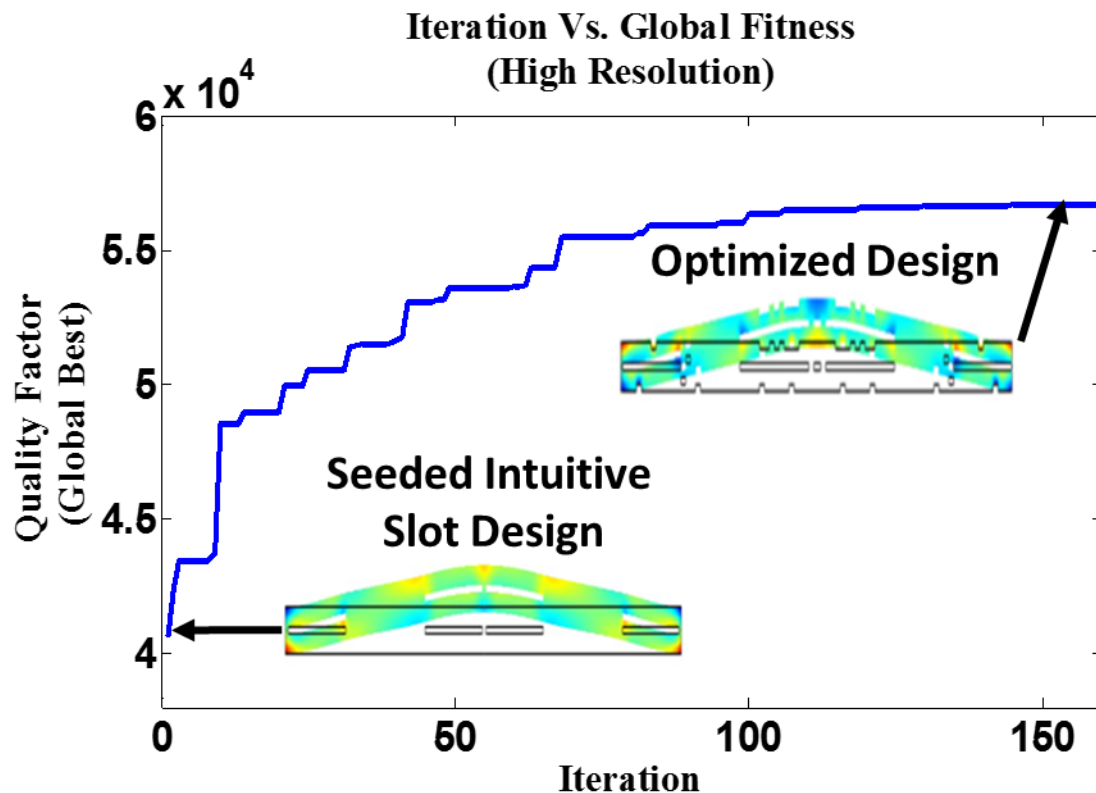
Figure 24: Global best Q_{TED} of swarm versus iteration value. Optimization is started at intuitive design and over 150 iterations the swarm converges on a design with a 40% improvement in Q_{TED}. Unlike the previous simulated BPSO optimization trials, this trial has the epi-seal design rules integrated into the algorithm

The intuitive design is seeded as a starting point for one of the agents. This is crucial, as if the intuitive design is not seeded the maximum Q simulated was observed to only reach approximately 40,000, which provides no improvement over the intuitive design. However, when knowledge of the intuitive design is leveraged and used as a starting location a 40% improvement in TED is simulated by the Binary particle swarm optimization. For this study we focused on three distinct designs. We designed resonators using the intuitive slotted design (simulated Q_{TED} of ~40,000), the Solid design (simulated Q_{TED}~10,000) and the BPSO design (simulated Q_{TED} of ~56,000). It should be noted the TED modeling for these designs was performed in 2D as 3D would have been prohibitively computationally expensive, more discussion on the differences in 2D simulations and 3D simulations will be explained in chapter 7.

Study Design: Anchor Loss

In order to experimentally validate our proposed anchor loss model, ring resonators were fabricated using the Stanford vacuum epi-seal process. The anchor structure design parallels the anchor structures of experimental gyroscopes, which often utilize a wine glass resonator mode attached to the substrate with a center post. Rings were scaled with various diameters in order to validate our modeling approach across a wide frequency range (~200 kHz – ~13 MHz) Figure 25.
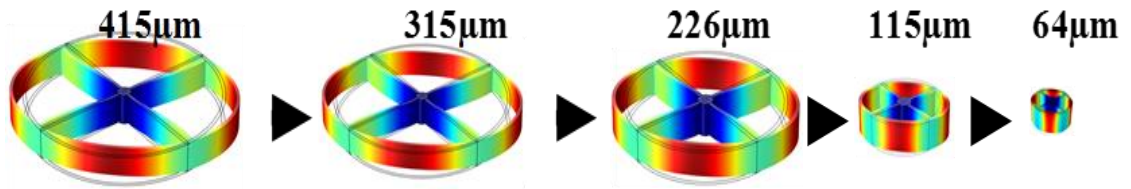
Figure 25: Scaled resonators anchored at the center post all dimensions are held constant except diameter which is scaled from 64 μm to 415 μm and the corresponding resonance frequency scales from 200kHz to 13 MHz.

Fabrication

Devices for both the TED optimization study and the scaled ring resonator study were fabricated at the Stanford Nanofabrication Facility by lab members of the Microstructures and Sensors laboratory. The SEM of Devices from each run are shown in Figure 26.
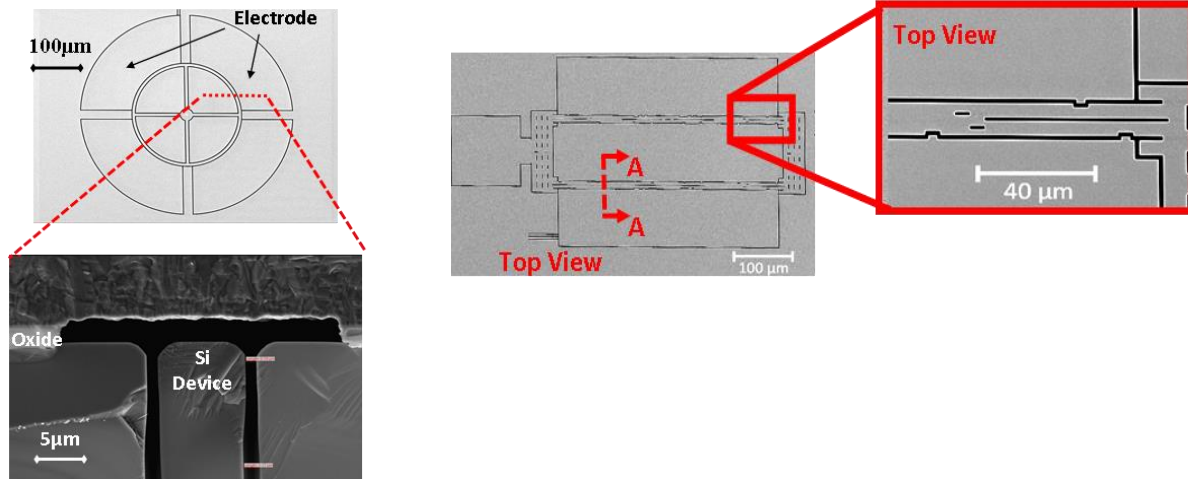
Figure 26: Left: SEM ring resonator from anchor loss study. Right: SEM optimized resonator for TED study

Chapter 7 Results

Devices were tested using an HP 4920A Network analyzer (Figure 27). Devices were electrostatically actuated and sensed. The force applied to released devices is described by equation 55.

$$F_{on\ ring} = F_1 - F_2 \approx \frac{C}{g}\left(V_{DC}V_{AC}\right) \tag{55}$$

The resulting motion causes a sense current that is then received by the Network analyzer (equation 56).

$$I_{Sense} = V_{DC}\frac{dC}{dt} \tag{56}$$

The frequency was swept and the resultant magnitude and phase plots were captured Figure 28. The measured Q signal magnitude was fit using a lorentzian function for the magnitude and Q_m is defined as the resonant frequency over the bandwidth at half maximum (-3dB). The measured Q phase was fit using an arc tangent function and Q_p is defined as the resonant frequency over bandwidth between -45 and -135 degrees.
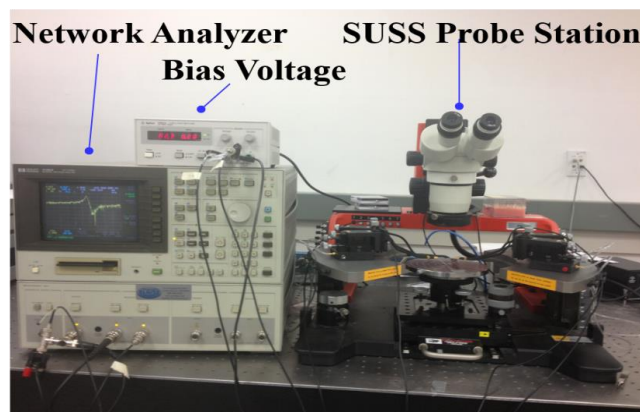
Figure 27: Measurement setup: HP4920A Network Analyzer, SUSS PM5 Probe Station and Agilent E3610A DC Power Supply
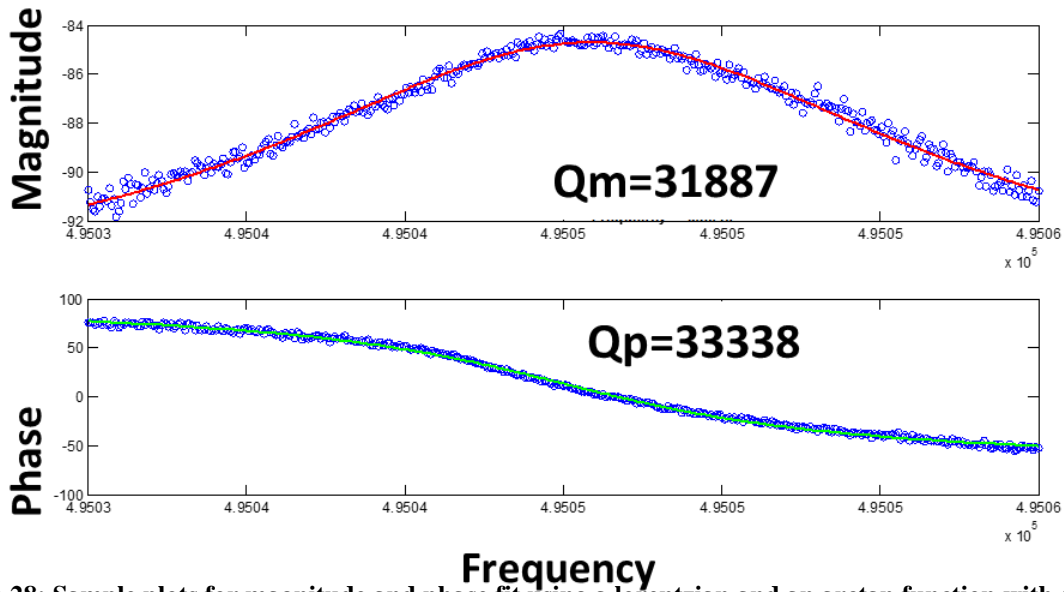
Figure 28: Sample plots for magnitude and phase fit using a lorentzian and an arctan function with Q_m and Q_p calculated from the respective fitted bandwidth

Thermoelastic Optimization

Using this technique 108 BPSO optimized devices were tested, 101 slotted beams and 27 solid beams. The summarized measured and simulated results are listed in Table 5. In Table 5, 2D reports 2D simulation values, 3D reports 3D simulation values, 3D+Anchor reports 3D simulation values where the heat transfer within the anchor is also included in the simulation and the measured results are reported last. The measured results and 3D+Anchor simulation results are displayed graphically in Figure 31.

Table 5 Measured and Simulated results. 2D reports 2D simulation values, 3D reports 3D simulation values, 3D+Anchor reports 3D simulation values where the heat transfer within the anchor is also included in the simulation and the measured results are reported last in all 108 BPSO devices, 101 slot devices and 28 solid devices were tested.

	SOLID	SLOT	BPSO
2D	10,000	40,000	56,000
3D	10,000	32,600	47,700
3D + Anchor	9,600	27,900	36,300
Measurement	**10,028±2000**	**26,408 ±2000**	**35,213±3000**

In order to interpret measured results it becomes necessary to account for all potential loss mechanisms that could affect measured Q.

Additional Damping Sources

In order to ensure that no additional damping mechanisms are present in these devices a thorough analysis of potential damping sources is required. While the epi-seal vacuum should negate air damping the three design types were measured in a vacuum chamber where pressure was controlled, in order to study and rule out any damping effects Figure 29.
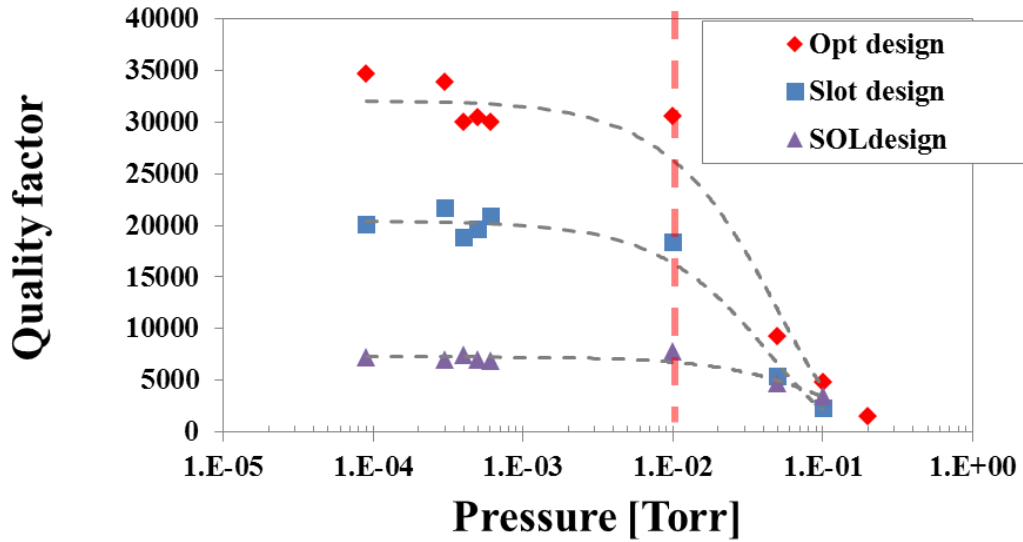
Figure 29: Pressure sweep for three design types, no appreciable air damping contribution is observed at the epi-seal pressure of ~10 mTorr.

Once we have ruled out any air damping effects, we must also rule out other potential dissipation mechanisms. Surface losses should be small as the surface area to volume ratio on these μm scale devices. Surface losses are most frequently observed in nanoscale resonators due to their high surface area to volume ratios [54]. Also the low frequency range of these devices rules out Akhieser or other local phonon dissipation mechanisms. The Qf product at 500 KHz is approximately 2e14 and the Akhieser limit is 4e8 [53]. The balanced tuning fork design should reduce clamping losses. Therefore the primary loss mechanism for these devices is most likely thermoelastic dissipation.

Ruling out other dissipation mechanisms, it is clear from the results in Table 5 that the 2D simulation does not capture the full thermoelastic effect and that when dominant thermal modes are suppressed (SLOT and BPSO design), heat transfer near the anchor becomes increasingly significant and cannot be ignored if accurate results are required. The additional anchor heat transfer effect is illustrated in Figure 30.

Figure 30: When the anchor is included in the simulation it allows for extra heat transfer lowering Q_{TED} and provides a more accurate simulation than when the anchor area is not included.

Results showing comparisons between Solid design, Intuitive slotted design and BPSO designs are shown in Figure 31. The simulated values shown are 3D simulations with anchor TED included. BPSO designs consistently performed 33% better than previous intuitive designs with minimal changes in resonant frequency.
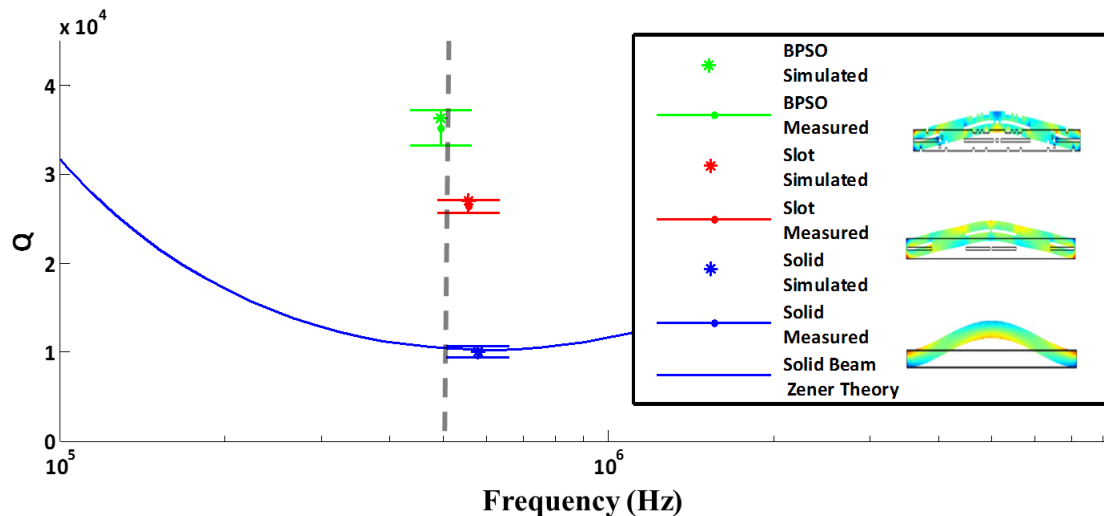
Figure 31: Q_{TED} using BPSO was measured to be 33% higher than the previous best intuitive design, which was measured in this fabrication run. There were 108 BPSO devices testes, 101 Slotted devices tested and 28 Solid devices tested. The error bars represent the standard deviation. The measured devices matched the target frequency within 1% of the 500 KHz target frequency with a standard deviation of 4KHz.

Thermoelastic Optimization Conclusions

The BPSO design method has been validated and has been shown to be an improvement over the intuitive design method due to its higher measured Q_{TED} and its flexibility in generating fabrication ready mask sets. This optimization scheme forms the foundation of a new best practices for finding practical designs with low TED for an arbitrary MEMS resonator. Through this work it is also concluded that 2D TED models are good for order of magnitude Q_{TED} prediction and optimization but break down with more

advanced designs. In these cases a full 3D model with anchor effects included is significantly more accurate.

Clamping Study

In our clamping study several device designs, with radii 64 μm, 115 μm, 215 μm 315 μm and 415 μm, were characterized and compared with simulated values (Figure 32). In order to compare experimental results to modeling, it is first necessary to identify the exact dissipation mechanisms for these ring resonators. Air damping was avoided with the vacuum encapsulation of the Stanford *epi-seal* process. Additionally, surface losses were likely negligible since the device dimensions provide a relatively low surface area to volume ratio compared to the nanoscale resonators where surface dissipation has been reported [54]. Also, at these lower frequency ranges (200 kHz-13 MHz) Akhieser, and Landau-Rumer are negligible as the QF product is approximately 2e14 [53]. Therefore, TED and clamping loss were the only two relevant dissipation mechanisms for these resonators.
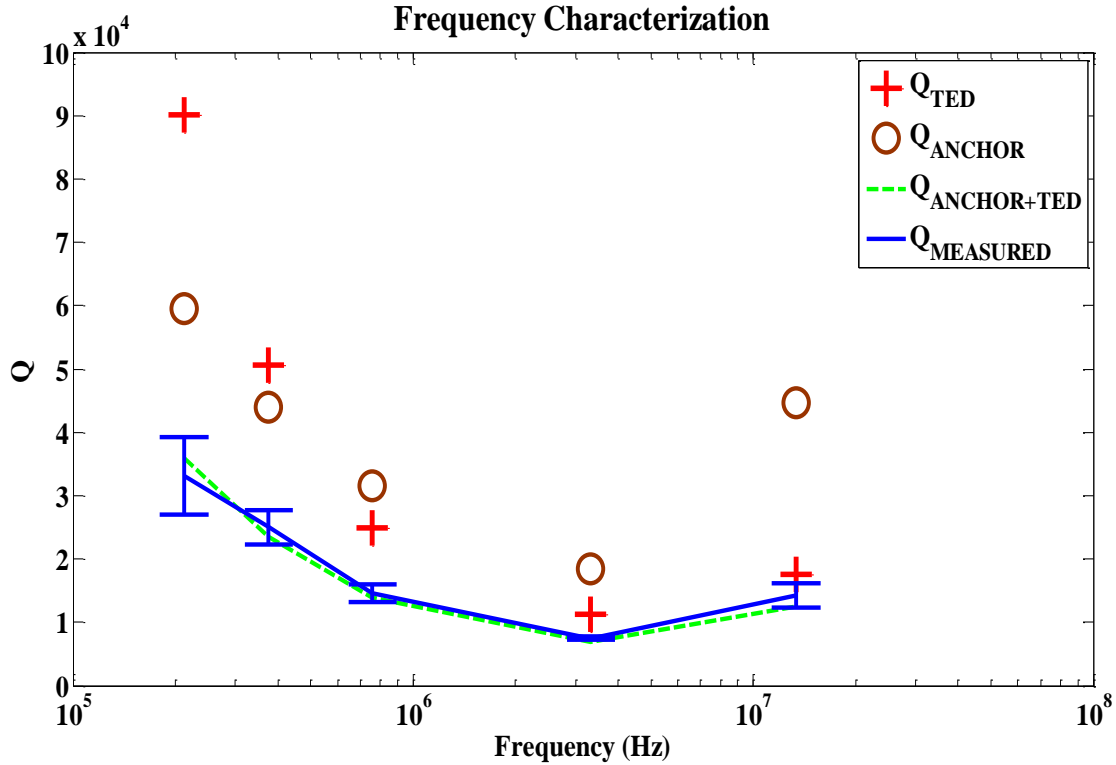
Figure 32: Plot of measured and simulated values of different dissipation mechanisms. Each data point represents 5 devices and error bars represent the standard deviation. Q_{TED} was solved using COMSOL thermal mechanical multiphysics package. The simulated Q is within 12% of the measured Q for all resonators.

Clamping Study Conclusions

This clamping study provides experimental validation of anchor loss models for an extensive range of low frequency (~200 kHz – ~13 MHz) devices. All measured designs, covering nearly two orders of magnitude in frequency, fell within 12% of the model's prediction Figure 32. This experimentally validated model provides a framework for designers to modify designs (e.g., stem length anchor design) in order to reduce anchor loss for arbitrary 3D geometries and identifies key process parameters (e.g., stress) for control of anchor losses. Continued improvement in the understanding of energy dissipation will greatly improve the design of high quality factor resonators for the design of high performance MEMS gyroscopes.

Chapter 8 Follow Up Studies

Thermoelastic Anchor Slot Heat Transfer Suppresion

After BPSO optimization the dominant thermal modes contributing to anchor loss are located at the

anchor shown below in Figure 33, reposted for reference from Figure 21 in Chapter 4.
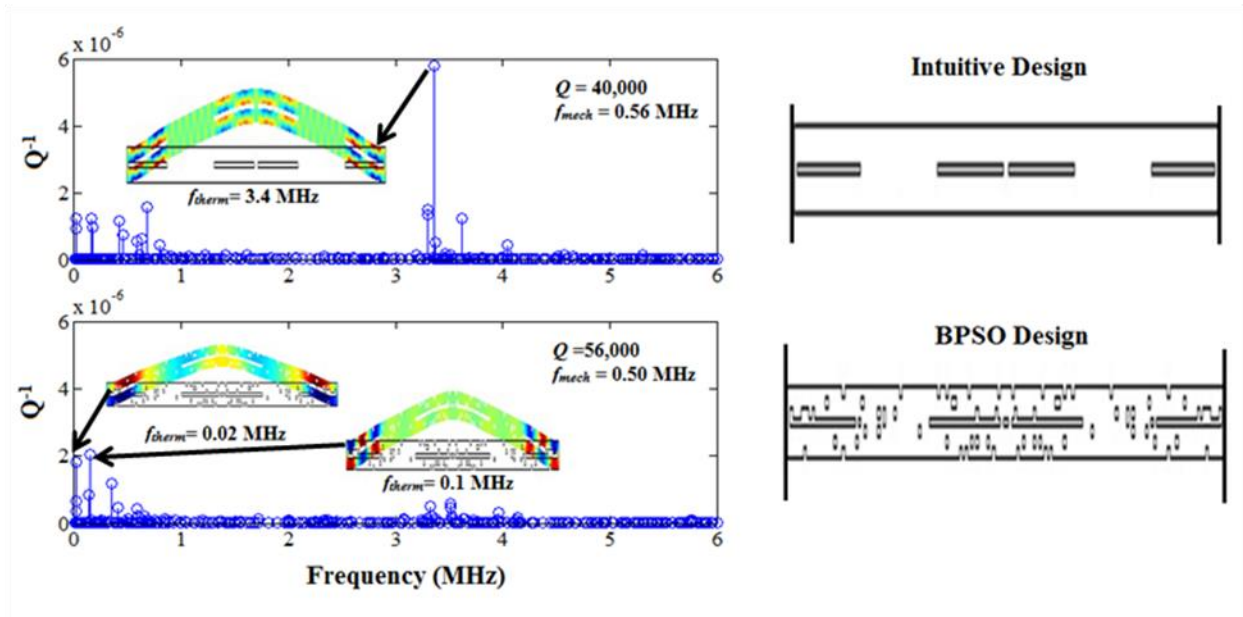
Figure 33: Comparison of the intuitive design approach (top) to the BPSO optimization (bottom) with low- and high-resolution optimizations. Thermal eigenmode stem plots are shown on the left, and resonator topologies are shown on the right. Stem plots show the contribution of each thermal eigenmode to Q, as determined by the weighting function in equation 7. Q values are simulated for the first 400 thermal modes in a fixed-fixed thermally insulated beam of dimensions 400 µm by 12 µm. Inset plots show dominant thermal modes. The top plot shows the design before optimization and the bottom plot shows the same beam after BPSO optimization where all thermal mode coupling has been suppressed except for the coupling at the anchor point.

In a follow up study devices were fabricated in order to suppress these remaining anchor modes, In

the original optimization the slot distance to the anchor was set to be 1 µm away from the anchor, this was

done in order to create a fixed stable anchor area. However, in simulation, if we extend this slot and cut

material into the anchor of a BPSO optimized beam, we can further suppress TED within the anchor

itself. Heat transfer can be blocked within the anchor for a simulated improvement of 6% in Q_{TED}.

Resonators were then fabricated to test for an improvement with slot lengths into the anchor from 1μm away from anchor to 2 μm into the anchor Figure 34.
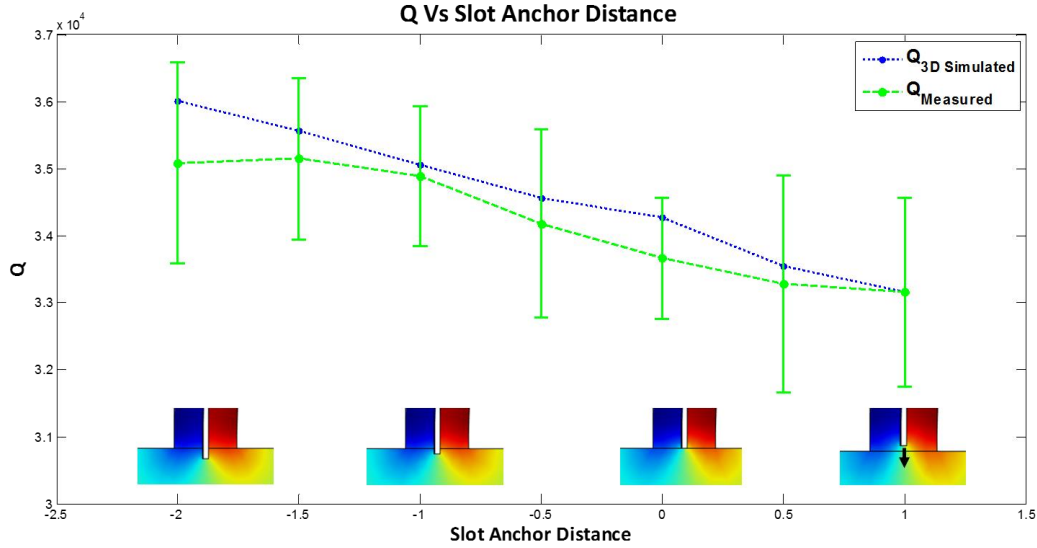
Figure 34: **Cutting an extended slot into the anchor of a BPSO optimized beam can help to decouple the thermal heat transfer at the anchor point. Simulated values here are performed in 3D with a very fine mesh to ensure accurate results (blue). The measured resonators include 16 tested at 1 μm, 12 at 0.5 μm, 13 at 0μm, 13 at -0.5 μm, 17 at -1 μm, 17 at -1.5 μm and 13 at μm with error bars reporting the standard deviation (green) show a ~5% improvement in Q_{TED} as predicted by simulation.**

Results from this study show that it is indeed possible to block the heat transfer at the anchor point with an extended slot into the anchor. This post optimization manual improvement technique shows how intuitive knowledge of TED in combination with the stochastic bio inspired optimization technique BPSO can be used to achieve the highest possible Q_{TED}. This work provides a new best practices for resonator design for low TED.
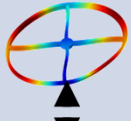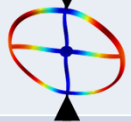
Anchor Loss Dissipation Coupling and Temperature Dependence Study

In Chapter 3 we proposed a new anchor loss theory that suggested anchor loss may have a temperature dependence due to coupling between anchor loss and other present dissipation mechanisms through the phase delay induced from damping between the reaction force and the velocity at the anchor point. This analysis suggests that anchor loss has the following form for our ring resonators equation 57

$$\frac{1}{Q_{Total}} = \alpha_{Anchor} \left(\frac{1}{Q_{TED}} \right)$$

(57)

Where the constant α_{Anchor}, will depend on anchor geometry but should remain relatively constant over temperature. In order to test this theory ring resonators were fabricated with three distinct resonator anchor designs shown below in Table 6. The ring resonators were anchored either at the center stem (Stem), a single side fixed anchor (SF) or a double side clamped ring where the anchor is positioned at nodal points with 180 degree separation.

Table 6 Three anchor designs were fabricated and tested in a cryo-probe station at room temperature 300K and cryogenic temperature 80K to study anchor losses at different temperatures. Additional damping other than TED is reported below each measurement in parenthesis.

	$Q_{Measured}$ 300 °K QTED=180,000	$Q_{Measured}$ 80 °K QTED~10^8	Anchor Design
Side Anchor ($Q_{other\ SF}$)	73,000 (122,803)	~175,000 (175,306)	
Double Anchor ($Q_{other\ DF}$)	65,469 (102,892)	500,000 (502,000)	
Stem Anchor ($Q_{other\ Stem}$)	107,000 (263,825)	1,280,000 (1.29e6)	

These results suggest that the additional damping mechanism in these resonators is in fact temperature dependent because the unaccounted for losses (in parenthesis) change dramatically with temperature. These unaccounted for losses are calculated by reciprocal subtraction of known dissipation from the measured Q equation 58.

$$\frac{1}{Q_{Other}} = \frac{1}{Q_{Measured}} - \frac{1}{Q_{TED}}$$

(58)

 Further results in Figure 35 show a comparison of a stem anchor design and a doubled fixed ring on the same die measured over a temperature range of 80K to 470K.
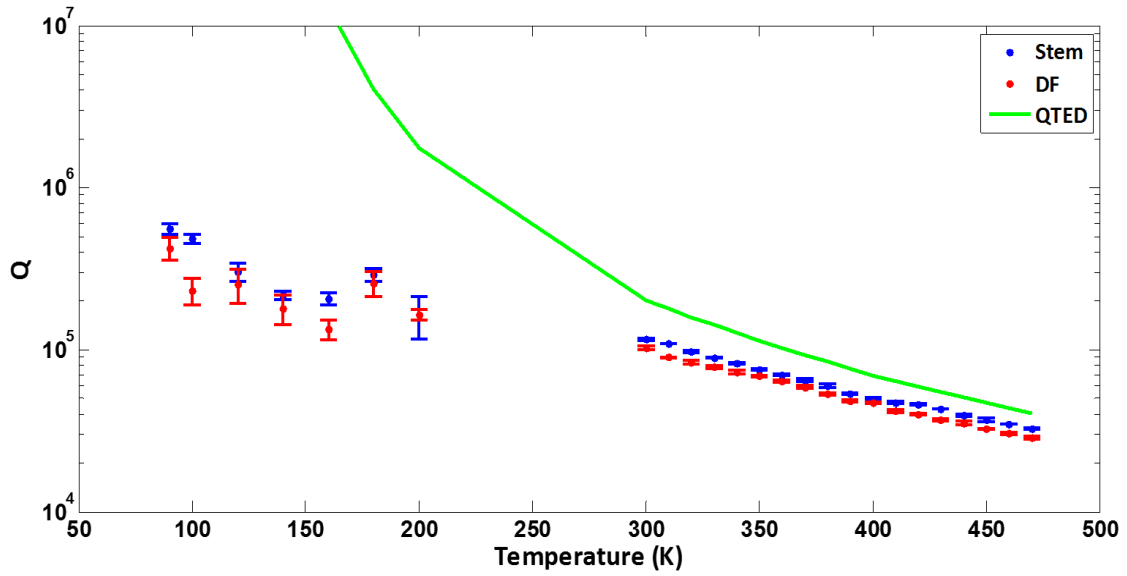
Figure 35: Dissipation of Stem anchored and Double Fixed ring resonators over temperature. Even at high temperatures anchor loss is not completely masked by TED. This is additional evidence of coupling. The jumps in data points at low temperatures were due to thermal stability challenges at low temperatures.

When we analyze these results we can assume that the damping in each of these resonators is the same except for the difference due to anchor loss for each design. Due to this, by extracting the Q_{Stem} Measurement from the Q_{DF} by reciprocal subtraction, as with parallel resistance, this additional Q_{Anchor} due to the double fixed anchors can be studied over temperature Figure 36.
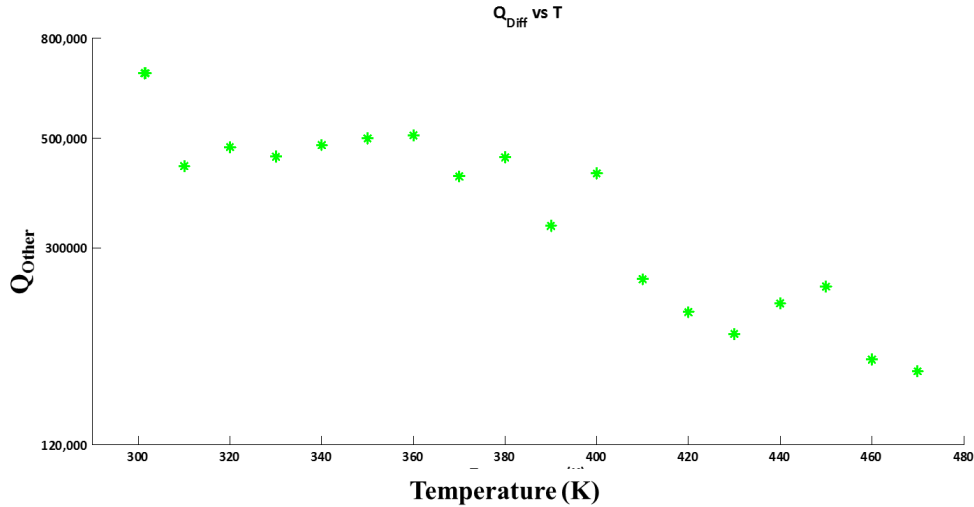
Figure 36: *Q_Other* **reports additional losses due to the double fixed anchor as compared to the stem anchor. The only difference between these devices is the type of anchor, Resonant frequency is within 100 Hz for stem and double fixed anchor devices therefore we suspect this additional loss to be due to anchor loss.**

These results also suggest that anchor loss does indeed have a temperature dependence like our theory suggests. However these results were very difficult to repeat as either the native oxide or surface contaminants were shown to be affecting the measurements on other tested devices. The data shown above was gathered in one continuous temperature sweep after a low temperature anneal in a constant ultra-high vacuum environment which provided stable measurements. This new anchor theory is still preliminary and the temperature dependence of Q_{Anchor} will continue to be an active area of research in the future.

Chapter 9 Conclusions

This work has reviewed fundamental theory of thermoelastic dissipation and provided a new best practices for high Q_{TED} design. Additionally, this work has introduced a novel anchor loss model that is general. Once the anchor surface is selected where the resonator is fixed to the substrate power flow through this surface can be used to calculate anchor loss. With the advancement in these modeling techniques and optimization MEMS resonator design should increasingly have less reliance on trial and error fabrication. Greater understanding of integrated Q modeling will identify the strengths and weaknesses of each approach can be appropriately analyzed.

BPSO optimization provides a flexible and efficient way to optimize resonators with low dissipation and produce fabrication ready mask sets. If the physics of dissipation can be accurately modeled then the resonator dissipation can be minimized using this approach. The use of networked agents in the BPSO allows us to leverage the power of swarm intelligence to explore potential design solutions. As is often the case with science, our natural world provides inspiration to unlock new and powerful technologies.

In terms of modeling advancements, new understanding of the significance of modeling the impact of resonator anchors on TED will increase the accuracy of TED modeling. For high Q_{TED} resonators the anchor must be included in the 3D TED simulations to ensure accurate results. Additionally, the continued advancement in the understanding and accurate modeling of anchor losses will continue to be an active area of study for years to come. The anchor loss model presented here shows promising initial results in using a direct calculation of anchor forces at the anchor junction. The accuracy of this direct modeling approach is not frequency dependent, which provides a significant advantage when compared to the current perfectly matched layer eigenmode approach to simulate anchor losses.

Appendix

Swarm Code

```
function [gqbest gbbest glambest qbesthist bbesthist bout]=swarm20sym(n, m, b)
%b is array of starting locations of each particle
%example: b{1}=[00000110000010101011101101010010101010101011010101010111010100...]
%n is the number of iterations the loop will run
%m is the number of particles in the swarm
i=1;
lam={};%frequency array
gqbest=0;%global best fitness value
qbest=[0];%best fitness value for each individual particle
qbesthist=[];%array of best global fitness after each iteration
gbbesthist={};%array of location of each best fitness
bbest={};%location of personal best fitness
gbbest=b{1};%location of global best fitness assumes best design is at b{1}
glambest=0;%frequency of globest fitness
[row col]=size(b{1});%number of rows and columns in b

reset=0;%reset is one if design has bad corners
resetb=zeros(1,m);%vector containing information on which particle needs to be reset
%initialize a random starting velocity for swarm
for p=1:m
    v{p}=rand(row,col)-0.5.*ones(row,col);
end




%initialize b1 (first fitness value)
%TEDgeomsym() is function that maps b(x) to beam and solves for QTED
[qbest(1) lam{1}]=TEDgeomsym(b{1});
gqbest=qbest(1);
gbbest=b{1};
bbest{1}=b{1};
%initialize rest of particles
```

```
for p=2:m
    [qbest(p) lam{p}]=TEDgeomsym(b{p});
end
bbest=b;


%loop for iterations
while (i<n)
    i=i+1;
%update posistion for each particle
for p=1:m

for j=1:col
    for k=1:row
        %if particle needs to be reset or this is the first iteration
        if (resetb(p)==1)||(reset==0)
        %update particle velocity
        v{p}(k,j)=v{p}(k,j)+rand()*(bbest{p}(k,j)-b{p}(k, j))+0.75*rand()*(gbbest(k,j)-b{p}(k,j));%edited for more
local searching
        %update posistion by comparing sigmoid to random number from -0.5 to 0.5
        b{p}(k,j)=round(1/(1+exp(-v{p}(k,j)-3))+(rand()-0.5));
        end
    end
end
end

reset=0;
resetb=zeros(1,m);

%check diagonals
{
for p=1:m
for k=1:row-1%no need to check last row
    for j=2:col%no need to check first column since will be set to one
        %check b1
        if(j~=col)%if j=col then only check left side
        if (b{p}(k,j)==0)%check first zero
            if (b{p}(k+1,j)~=0)%if number directly below the current zero is zero then diagonals are okay no need to
check
                if (b{p}(k+1,j+1)==0)%check bottom right
                resetb(p)=1;
                reset=1;
                break;
            else if (b{p}(k+1,j-1)==0)%check bottom left
                resetb(p)=1;
                reset=1;
                break;
                end
                end
            end
        end
        else if (j==col)%if you are in last row only check the bottom left
            if (b{p}(k+1,j-1)==0)
            resetb(p)=1;
            reset=1;
            break;
```

```
            end
          end
        end



          end
        end
end
if (reset==1)
    i=i-1;%if something needs to be reset then decrease iteration and restart loop
    continue;
end

%check if there is a new q best local and global
for p=1:m
[q(p) lam{p}]=TEDgeomsym(b{p});
%check/compare local best
if(q(p)>qbest(p))
    qbest(p)=q(p);
    bbest{p}=b{p};
%check/compare global best
    if(q(p)>gqbest)
        gqbest=q(p);
        gbbest=b{p};
        glambest=lam{p};
    end
end
end

%document history
qbesthist=[qbesthist gqbest];
bbesthist{i}=gbbest;
%output certain variables to check progress
i
gbbest
gqbest
glambest
end
bout=b;%document final particle positions to access convergence
```

References

[1] J. C. Eloy, E. Mounier, and P. Roussel, *Advanced Microsystems for Automotive Applications 2005*. Berlin, Heidelberg: Springer, 2005.

[2] R. Neul, U. M. Gomez, K. Kehr, W. Bauer, J. Classen, C. Doring, E. Esch, S. Gotz, J. Hauer, B. Kuhlmann, C. Lang, M. Veith, and R. Willig, "Micromachined Angular Rate Sensors for Automotive Applications," *Sensors Journal, IEEE,* vol. 7, pp. 302-309, 2007.

[3] A. Partridge, M. Lutz, B. Kim, M. Hopcroft, R. N. Candler, T. W. Kenny, K. Petersen, and M. Esashi, "MEMS Resonators: Getting the Packaging Right," in *SEMICON-Japan*, 2005.

[4] L. Lin, C. T.-C. Nguyen, R. T. Howe, and A. P. Pisano, "Microelectromechanical filters for signal processing," *MEMS,* pp. 226-231, 1992.

[5] C. T.-C. Nguyen, L. P. B. Katehi, and G. M. Rebeiz, "Micromachined Devices for Wireless Communications," *Proceedings of the IEEE,* vol. 86, pp. 1756-1768, 1998.

[6] R. Ruby, P. Bradley, D. Clark, D. Feld, T. Jamneala, and W. Kun, "Acoustic FBAR for filters, duplexers and front end modules," in *Microwave Symposium Digest, 2004 IEEE MTT-S International*, pp. 931-934, 2004.

[7] H. Chandrahalim, D. Weinstein, C. Lih Feng, and S. A. Bhave, "Channel-Select Micromechanical Filters Using High-K Dielectrically Transduced MEMS Resonators," in *19th IEEE International Conference on Micro Electro Mechanical Systems*, pp. 894-897, 2006.

[8] D. Weinstein and S. A. Bhave, "Internal Dielectric Transduction in Bulk-Mode Resonators," *Microelectromechanical Systems, Journal of,* vol. 18, pp. 1401-1408, 2009.

[9] G. Piazza, P. J. Stephanou, and A. P. Pisano, "Single-Chip Multiple-Frequency ALN MEMS Filters Based on Contour-Mode Piezoelectric Resonators," *Microelectromechanical Systems, Journal of,* vol. 16, pp. 319-328, 2007.

[10] M. Rais-Zadeh and F. Ayazi, "Small-bandwidth integrated tunable bandpass filters for GSM applications," in *IEEE 21st International Conference on Microelectromechanical Systems*, pp. 1032-1035, 2008.

[11] F. Ayazi, "MEMS for integrated timing and spectral processing," in *Custom Integrated Circuits Conference, 2009. CICC '09. IEEE*, 2009, pp. 65-72.

[12] P. S. Waggoner and H. G. Craighead, "Micro- and nanomechanical sensors for environmental, chemical and biological detection," *Lab on a Chip,* vol. 7, pp. 1238-1255, 2007.

[13] T. P. Burg, M. Godin, S. M. Knudsen, W. Shen, G. Carlson, J. S. Foster, K. Babcock, and S. R. Manalis, "Weighing of biomolecules, single cells and single nanoparticles in fluid," *Nature,* vol. 446, pp. 1066-1069, 2007.

[14] H. Zhang, M. S. Marma, S. K. Bahl, E.-S. Kim, and C. E. McKenna, "Sequence Specific Label-Free DNA Sensing Using Film-Bulk-Acoustic-Resonators," *Sensors Journal, IEEE,* vol. 7, pp. 1587-1588, 2007.

[15] A. Lin, Y. Hongyu, M. S. Waters, E.-S. Kim, and S. D. Goodman, "Explosive trace detection with FBAR-based sensor," in *IEEE 21st International Conference on Microelectromechanical Systems*, pp. 208-211, 2008.

[16] H. J. Lee, K. K. Park, O. Oralkan, M. Kupnik, and B. T. Khuri-Yakub, "CMUT as a chemical sensor for DMMP detection," in *2008 IEEE International Frequency Control Symposium,* pp. 434-439, 2008.

[17] H. Wohltjen, A. W. Snow, W. R. Barger, and D. S. Ballantine, "Trace Chemical Vapor Detection Using SAW Delay Line Oscillators," *IEEE Transactions on Ultrasonics, Ferroelectrics and Frequency Control,* vol. 34, pp. 172-178, 1987.

[18] L. Yang, L. Wei-Chang, R. Zeying, and C. T. C. Nguyen, "A resonance dynamical approach tofaster, more reliable micromechanical switches," in *Frequency Control Symposium, 2008 IEEEInternational*, pp. 640-645, 2008.

[19] K. Akarvardar, D. Elata, R. T. Howe, and H. S. P. Wong, "Energy-Reversible Complementary NEM Logic Gates," in *Device Research Conference,* pp. 69-70, 2008.

[20] Y. T. Yang, C. Callegari, X. L. Feng, K. L. Ekinci, and M. L. Roukes, "Zeptogram-Scale Nanomechanical Mass Sensing," *Nano Letters,* vol. 6, pp. 583-586, 2006.

[21] K. L. Ekinci, M. H. Huang, and M. L. Roukes, "Ultrasensitive nanoelectromechanical mass detection," *Appl. Phys. Lett.,* vol. 84, pp. 4469-4471, 2004.

[22] D. Rugar, R. Budakian, H. J. Mamin, and B. W. Chui, "Single spin detection by magnetic resonance force microscopy," *Nature,* vol. 430, pp. 329-332, 2004.

[23] A. D. O'Connell, M. Hofheinz, M. Ansmann, R. C. Bialczak, M. Lenander, E. Lucero, M. Neeley,D. Sank, H. Wang, M. Weides, J. Wenner, J. M. Martinis, and A. N. Cleland, "Quantum ground state and single-phonon control of a mechanical resonator," *Nature,* vol. 464, pp. 697-703, 2010.

[24] T. Rocheleau, T. Ndukum, C. Macklin, J. B. Hertzberg, A. A. Clerk, and K. C. Schwab, "Preparation and detection of a mechanical resonator near the ground state of motion," *Nature,* vol. 463, pp. 72-75, 2010.

[25] C.Zener, "Internal friction in solids:I. Theory of internal friction in reeds," *Phys. Rev.,* vol.52, p.230, 1937.

[26] C.Zener, "Internal friction in solids:II General theory of thermoelastic internal friction," *Phys. Rev.,* vol. 53 p.90, 1938.

[27]Nowacki, *Thermoelasticity*. Elmsford, NY: Pergamon, 1962.

[28] S.P. Timoshenko, J.N. Goodier *Theory of Elasticity* (*3rd. edn.)*McGraw-Hill, New York p. 140 1970

[29] A. Duwel, R. N. Candler, T. W. Kenny and M. Varghese, "Engineering MEMS Resonators With Low Thermoelastic Damping," *J. Microelectromech, Syst.,* vol. 15, No. 6, pp1437-1445, 2006.

[30] S. Chandorkar, R. N. Candler, A. Duwel R. Melamud, M. Agarwal, K. E. Goodson and T. W. Kenny,"Multimode thermoelastic dissipation," *J. of Appl. Physics*, Vol. 105, 2009.

[31] S. Zotov, B. Simon, I Prikhodko A. Trusov and A. Shkel "Quality factor Maximization through Dynamic Balancing of Tuning Fork Resonator," *Sensors Journal IEEE*   Vol. 14 No. 8 pp.2706-2714 April 2014.

[32] D. Bindel, E.Quèvy, T. Koyama, S. Govinjee, J. W. Demmel and R. T. Howe, "Elastic PMLs for resonator anchor loss simulation," *Int; J. Num Meth Eng.,* Vol. 64, No. 6, pp. 789-818, Aug 2005.

[33] R. N. Candler, et al., "Long-Term and Accelerated Life Testing of a Novel Single-Wafer Vacuum Encapsulation for MEMS Resonators," JMEMS, Vol. 15, No. 6, pp. 1446-1456, 2006.

[34] J. Lake, Y.-H. Hwang, E. Ng, C.-H. Ahn, V. Hong, Y. Yang, Y. Dai, and R. Candler, "Experimental Validation of 3D Intuitive Modeling Approach for Anchor Loss in MEMS Resonators," *Solid-State Sensors, Actuators, and Microsystems Workshop, Hilton Head* , pp. 277-280 (2014)

[35] A. S. Nowick and B. S. Berry, Anelastic Relaxation in Crystalline Solids (1972)

[36]K. E. Peterson "Silicon as a Mechanical Material" *Proceedings of The IEEE*, Vol. 70, No. 5, MAY 1982.

[37] Franz, Aermer, and Andrea Schilp. Method of Anisotropically Etching Silicon. Laermer, Franz and Schilp, Andrea, assignee. Patent 5501893. Mar. 1996.

[38] https://www.comsol.com/

[39] Bendsøe, "Optimal shape design as a material distribution problem," *Structural Optimization,* vol. 1, pp. 193-202, 1989.

[40] D. Peng, B. Merriman, S. Osher, H. Zhao, and M. Kang, "A PDE-Based Fast Local Level Set Method,"*Journal of Computational Physics* vol. 155 no.2 pp. 410-438 1999.

[41] K. Svanberg, "The Method Of Moving Asymtotes-A New Method For Structural Optimization,"*Journal of numerical methods in Engineering* vol. 24 pp. 359-373 1987

[42] K. Deb, A. Pratap, S. Agarwal, and T. Meyarivan, "A Fast and Elitist Multiobjective Genetic Algorithm: NSGA-II," *IEEE Transactions On Evolutionary Computing*, pp 182-197 2002.

[43] R. S. Parpinelli, H Lopes, and A. Frietas, "Data Mining With an Ant Colony Optimization Algorithm," *IEEE Transactions On Evolutionary Computing*, vol. 6 no. 4 pp 321-332 2002.

[44] S. Kirkpatrick, "Optimization by Simulated Annealing: Quantitative studies," *Journal of Statistical Physics,* vol. 34 no. 5 1984.

[45] J. Kennedy and R. Eberhart, "Particle swarm optimization," *IEEE International Conference on Neural Networks,* 1995.

[46] R. N. Candler, et al. "Impact of geometry on Thermoelastic Dissipation in Micromechanical Resonant Beams," Journal of Micromechanical Resonant Beams," Journal of Microelectromechanical systems, vol. 15, pp. 927-934, 2006.

[47] N. Jin and Y. Rahmat-Samii, "Advances in particle swarm optimization for antenna Designs: real number, Binary, single objective and Multi objective implementations," *IEEE Trans. Antennas propag.* vol. 55 no. 3 pp.556-567 Mar. 2007.

[48] Shirin Ghaffari, Eldwin Jiaqiang Ng, Chae Hyuck Ahn, Yushi Yang, Shasha Wang, Vu A. Hong, and Thomas W. Kenny, "Accurate Modeling of Quality Factor Behavior of Complex Silicon MEMS Resonators," Journal of Microelectromechanical Systems, Vol. 24, No. 2, pp. 276-288, Apr 2015.

[49] A. B. Graham, et al., "A Method for Wafer-Scale Encapsulation of Large Lateral Deflection MEMS Devices," JMEMS, Vol. 19, No. 1, pp. 28-37, 2010.

[50] http://www.sitime.com/news/436-sitime-enters-smartphone-market-with-first-mems-oscillator

[51] **]** J. Lake, , E. Ng, C.-H. Ahn, V. Hong, Y. Yang, J. Wong and R. Candler, "Particle Swarm Optimization for Design of MEMS resonators with low Thermoelastic Dissipation," *International Transducers-Eurosensors*, Barcelona 2013

[52] R. N. Candler, et al., "Long-Term and Accelerated Life Testing of a Novel Single-Wafer Vacuum Encapsulation for MEMS Resonators," JMEMS, Vol. 15, No. 6, pp. 1446-1456, 2006.

[53] S. Ghaffari, S. Chandorkar, S. Wang, E. Ng, C. Ahn, V. Hong, Y. Yang and T. Kenny "Quantum limit of Quality Factor in Silicon Micro and Nano mechanical Resonators" *Nature Scientific Reports* Vol. 3 No. 3244.

[54] J. A. Henry, Y. Wang, D. Sengupta and M. A. Hines. "Understanding the Effects of Surface Chemistry on Q: Mechanical Energy Dissipation in Alkyl-Terminated(C_1-C_{18}) Micromechanical Silicon Resonators," *Journal of Physical Chemistry B*. vol. 111 pp. 88-94, Jan 2007